STUDY OF DC AND PULSED CORONA DISCHARGES IN GASES, VAPORS AND LIQUIDS FOR PHASE-CHANGE HEAT TRANSFER APPLICATIONS

A Thesis

by

KARAN JAKHAR

Submitted to the Office of Graduate and Professional Studies of
Texas A&M University
in partial fulfillment of the requirements for the degree of

MASTER OF SCIENCE

Chair of Committee,	Dion S. Antao
Committee Members,	David Staack
	Christopher Limbach
Head of Department,	Bryan Rasmussen

December 2020

Major Subject: Mechanical Engineering

ABSTRACT

A plasma can produce highly energetic and chemically active species making it attractive for industrial applications. In this work we investigate both, the DC negative plasma discharges at lower discharge currents (0-0.8 mA), and a negative pulsed corona discharge. DC plasma discharges in a pin-to-plate electrode configuration were electrically, optically and spatially characterized for various plate electrodes (anodes): solids as well as liquids. The negative corona discharge regime and a non-stationary filamentary glow discharge regime were observed with an additional intermediate streamer-spark discharge regime depending on the surface roughness and the discharge gap for solid anodes. The negative corona discharge regime was observed to have a conical diffuse glow region close to the anode for solid and polar liquid anodes.

Solid anode surfaces treated in this negative corona discharge regime (with a diffuse glow) were observed to have a change in wettability and an increase in roughness. Imaging revealed the formation of micro/nanostructures with poor adhesion to substrates of Au, Pt and Si. X-ray photoelectron spectroscopy measurements revealed oxidation of the anode materials. Unlike Au, Pt and Si, thin metals films of Al, Cu and Ni were damaged potentially due to a moving constriction within the diffuse glow region. We hypothesize that this constriction likely oxidized the anode surface resulting in metal oxides that do not adhere well to their parent metals. Further research is required to understand the local surface chemistry within the diffuse glow.

A double spark gap pulse generator was built and used to generate nano-to-microsecond pulsed corona discharges in air, and fluid vapor and liquid phases. The circuit was characterized for the magnitude of the pulse discharge voltage and pulse duration, at atmospheric and sub-atmospheric pressures. This pulsed negative corona discharge may be leveraged to make accurate, local and non-contact measurements in phase change heat transfer processes, both for temperature and species diagnostics.

DEDICATION

I would like to dedicate this thesis to my mother and father for their endearing support.

ACKNOWLEDGEMENTS

Foremost, I would like to express my sincere gratitude to my advisor Dr. Antao for continuous support of my MS study and research, for his patience, enthusiasm and immense knowledge.

Besides my advisor, I would like to thank my committee members, Dr. Staack and Dr. Limbach, for their guidance and support throughout the course of this research.

I am thankful to my undergraduate advisor at Indian Institute of Technology Patna, Dr. Raj for providing me the first platform to conduct impactful research.

I thank my fellow lab mates of Thermal Engineering Group: Ruisong Wang for his help to make this thesis a reality; Sanat Kumar and Sunil Kumar for stimulating discussions; Martin Quezada, Shaoib Ahmed and Minlin Lyu for assisting me in fabrication of the experimental setup.

Thanks also go to my friends and colleagues and the department faculty and staff for making my time at Texas A&M University a great experience.

I thank J. Mike Walker ’66 Department of Mechanical Engineering at Texas A&M University for funding to support my graduate study.

This work was also made possible in part by U.S. Department of Energy, Office of Energy Efficiency and Renewable Energy, Geothermal Technologies Office (GTO) under award DE-EE0008605.

Finally, thanks to my mother and father for their encouragement and support.

CONTRIBUTORS AND FUNDING SOURCES

Contributors

This work was supervised by a thesis committee consisting of Dr. Dion Antao (advisor), Dr. David Staack of J. Mike Walker ’66 Department of Mechanical Engineering and Dr. Christopher Limbach of Department of Aerospace Engineering.

Atomic Force Microscopy (AFM) and X-ray Photoelectron Spectroscopy (XPS) measurements were conducted by Ruisong Wang of J. Mike Walker ’66 Department of Mechanical Engineering.

All other work conducted for the thesis was completed by student independently.

Funding Sources

Graduate study was supported by J. Mike Walker ’66 Department of Mechanical Engineering at Texas A&M University.

This work was also made possible in part by U.S. Department of Energy, Office of Energy Efficiency and Renewable Energy, Geothermal Technologies Office (GTO) under award DE-EE0008605.

NOMENCLATURE

T_i	Temperature of ions
T_e	Temperature of electrons
T_o	Translational temperature
T_r	Rotational temperature
T_v	Vibrational temperature
DG	Discharge gap
OES	Optical emission spectroscopy
I_d	Discharge current
V_d	Discharge voltage
V_{DC}	Power source voltage
R_s	Shunt resistance
R_b	Ballast resistance
NCD	Negative corona discharge
S-SD	Streamer-spark discharge
N-SFGD	Non-stationary filamentary glow discharge
TR	Transitional regime

TABLE OF CONTENTS

Page

LIST OF FIGURES

Page

LIST OF TABLES

Page

1. INTRODUCTION

1.1. Plasma Discharges

Plasma is estimated to constitute more than 99% of the visible universe: the solar corona, solar wind, nebula, Earth's ionosphere and lightning in Earth's atmosphere [1]. As temperature increases, molecules become more energetic and transform matter in the sequence of solid, liquid, gas and finally plasma, a "distinct fourth state of matter". Plasma is an ionized gas containing free electric charges – both electrons and ions, making them electrically conductive and strongly responsive to electromagnetic fields. An ionized gas is usually called plasma when it is electrically neutral.

A plasma can produce highly energetic and chemically active species (e.g., ions, electrons, radicals and excited states) and can be in thermodynamic non-equilibrium, forming high concentrations of the chemically active species at low bulk temperatures (as low as room temperature). These features are attractive for industrial applications and laboratory made plasma have provided applications in thermonuclear synthesis, electronics fabrication, lasers and florescent lamps [2-4].

The temperature in plasmas (similar to gases) is determined by the average energies of the plasma particles (neutral and charged, T_i for ions and T_e for electrons) and their relevant degrees of freedom (translational (T_o), rotational (T_r) and vibrational (T_v)). Based on these temperatures/modes of internal energy, plasma discharges are broadly classified into thermal and non-thermal discharges. The electron temperature (T_e) is usually higher than that of heavy particles (T_o), and subsequent collision of electrons with

heavy particles can equilibrate their temperatures. The quasi-equilibrium plasma where the temperature of the electrons and heavy particles approach each other ($T_e \approx T_v \approx T_r \approx T_i \approx T_o$) is usually called a thermal plasma. If time and energy are not sufficient for the equilibration of T_e and T_o, T_e often increases T_o. Ionization and chemical processes in such non-equilibrium plasmas are directly determined by the electron and vibrational temperatures and, therefore are not sensitive to thermal processes and temperature of the gas. This non-equilibrium plasma is usually called a non-thermal plasma ($T_e > T_v > T_r \approx T_i \approx T_o$) with T_e about 1 eV (~10,000 K) and the bulk gas temperature close to the ambient temperature [1].

1.2. Motivation

In this work we are studying the negative corona discharge (both dc and pulsed excitation) for potential application as (1) a probe for metrology, (2) an enhancement technique, in liquid-vapor phase-change heat transfer systems, and (3) surface modification.

Non-contact temperature metrology at and near the liquid-vapor interface during phase-change heat transfer is non-trivial and lacking in the phase-change heat transfer literature. In the past, thermocouples have been widely used to measure temperature at/near liquid-vapor interface [5-9]. These thermocouples are found to overestimate the temperature at/near liquid-vapor interface, measured in vapor by almost 50% [5]. This is attributed to the conduction heat transfer in thermocouple wires to the probe, inaccessibility of the interface as a result of experimental limitation and rarefaction of vapor causing different temperatures at the probe and the liquid-vapor interface. DC

negative corona discharges in air have been observed to have a “diffuse glow” near the anode [10-12], however, the mechanism for its existence is not well understood. Temperature measured employing optical emission spectroscopy (OES) of the diffuse glow region showed lower rotational temperatures close to the ambient temperature. The low rotational temperature (potentially lower in pulsed excitation modes) makes the discharge attractive for non-contact temperature metrology at and near the anode surface with potential applications in phase change heat.

Spectroscopic temperature measurements from literature indicate higher vibrational temperature in the diffuse glow region of DC negative corona discharges [10] indicating the presence of active species which may potentially be used for surface modification. Furthermore, the material under the diffuse glow region appears to be oxidized, which may be the result of higher chemical activity due to higher vibrational temperatures in this region. Hence corona discharges can change the surface morphology of materials, and originally smooth surface can become rough [13-15]. Additionally, the wettability of surfaces can be modified by treating these surfaces with corona discharges [16, 17] and subsequently treatment with corona discharges also improves adhesion of thin films [18-20]. An understanding of the diffuse glow present in negative corona discharges is still in its preliminary stages, and a better understanding can facilitate its use in different applications.

Condensation heat transfer plays an important role in a variety of high-efficiency heat exchangers, such as heat pipes, and refrigeration and air conditioning radiators. A small amount of non-condensable gas added to pure vapor can greatly affect the

condensation heat transfer coefficient. Studies show that the presence of NCG play a large (detrimental) role by reducing the heat transfer coefficient in liquid-vapor phase-change heat transfer processes [21-23]. While most phase-change heat transfer studies attempt to reduce the presence of NCGs in the test systems, accurate *in-situ* quantification capabilities for these NCG species do not exist [24, 25]. NCG's are traditionally measured using pressure gauges [26, 27] and this limits the measurement of species concentration (NCGs) to ~4000 ppm [24]. Non-thermal pulsed corona discharges and optical emission spectroscopy can also be leveraged to detect species in a fluid. Nanosecond duration pulses can be used to detect species concentrations upto 1 ppm in femtolitres of liquid volume [28] enabling a promising prospect to make accurate, local and non-contact measurement in phase-change heat transfer systems for quantification of dissolved NCGs.

1.3. Background and Literature Review

1.3.1. Corona Discharges

Corona discharges are characterized with non-uniform strong electrical field, ionization and luminosity around an electrode. The electrode is usually a sharp point or edge. Corona discharges requires high voltage for ignition around a single electrode, the rest of discharge gap (DG) is dark with low electric field. If the voltage grows higher the remaining dark part of DG also breaks down and the corona is transformed in to sparks [1]. The mechanism for sustaining the continuous ionization level in a corona discharge depends on the polarity of electrode where the high electric field is located. A corona discharge with high electric field zone is concentrated around the anode, the discharge is referred as positive corona. Conversely, the negative corona has high electric field zone

around the cathode. Ignition of corona is dictated by Townsend mechanism [29]. The applied electric field accelerates oppositely charged particles in opposite directions, separating them and preventing their recombination. Electrons with higher charge to mass ratio accelerate at higher velocity than positive ions and gains enough energy to ionize another atom/molecule upon collision, displacing electron and form a positive ion in the process. These secondary ions are accelerated and the electron collides with other atoms, creating further electron-positive ion pairs causing a chain reaction process called electron avalanche. The glow or luminosity of coronas discharges is caused by electron recombination with positive ions to form neutral atoms releasing photons in the process. In negative corona, the ions are attracted inwards while the electrons are repelled outwards from the pin electrode. The avalanche mechanism cannot be sustained at a certain distance from the pin electrode since the electric field isn't high enough to facilitate collision-based electron impact ionization. In this dark region the ions and electrons move through the air eventually reaching the opposite electrode to complete the circuit [30].

Ability of corona discharges to generate high concentration of active species at atmospheric pressure without heating up the gas volume have made them appealing to different modern industrial applications, such as electrophotographic printing [31], electrostatic precipitation [32], abatement of Volatile Organic compounds [33], atmospheric pressure ionization mass spectrometry [34] ozone synthesis [35-37], detoxifying chemical warfare gases [38] and medical applications [39-41].

For corona discharges in pin to plate geometry, the initial form will be the Trichel pulse corona [42, 43], followed by pulseless continuous corona and spark discharge with

increasing discharge voltage [44]. In Trichel pulse mode negative corona discharges operate at relatively low voltage values. The pulse duration is short (100s of nano-seconds) with mean currents in tens of micro-amperes. The pulses for negative corona disappear in contrast to the case of positive corona where they exist till transition to spark [30]. From Trichel pulses the corona discharges transition to pulseless glow mode [45], where a Faraday dark space, a conical shaped positive column and another dark space between the positive column and the plate electrode are observed. This mode is generally observed in the presence of gas flow for DC negative corona discharges [11, 12]. Anode surfaces have been reported to oxidize and observed to deposit thin films in this region. At atmospheric pressures in air the DC negative corona discharge has been reported to transition to transient spark followed by the non-stationary filamentary glow discharge [12], which has been reported to look like a dancing discharge with a pink current filament moving chaotically in the DG due to convection of the background gas heated by this filament.

1.3.2. Pulsed Corona Discharges

In recent years, the research of plasmas in liquids has broadened to address variety of applications including chemical analysis [46], shockwave production [47], nanomaterial synthesis [48, 49], extraction of bio compounds [50], high voltage machining [51], water treatment [47, 52] and medicine for wound healing, skin treat, dentistry and cancer treatment [53, 54].

Many studies in the literature on plasma parameters use OES technique, which can be applied in many fields, from astrophysical plasmas [55] to laboratory experiments such as nuclear fusion [56] and plasma assisted material processing [57-60]. OES of non-

thermal nanosecond pulsed corona discharges can be leveraged to detect species in a fluid with concentrations upto 1 ppm in femtolitres of liquid volume [60]. Depending on the pulse intensity, a thermal plasma can form, increasing the electron density and degree of liquid dissociation [61-63]. This results in broadening of hydrogen line hiding the presence of other elemental and spectral lines [64-66]. Short voltage pulses and short rise time of non-thermal nanosecond pulsed corona discharges do not affect the phenomenon occurring, facilitating the detection of multiple elements simultaneously without altering the medium.

1.4. Thesis Overview

Beyond the introduction in Chapter 1, this thesis is organized as follows: Chapter 2 and Chapter 3 contains the presentation of results. Chapter 3 is focused on atmospheric DC negative corona discharges in air on solid and liquid anodes. The chapter includes voltage-current characteristics, discharge visualization, roughness measurements and X-ray photoelectron spectroscopy (XPS) measurements for each anode with varying DG. A set of experiments also includes discharges at lower pressure. Chapter 3 comprises of pulsed corona discharges in air, water vapor and varying extent of degassed water. Current amplitude and discharge pulse width are facilitated by a double spark gap setup, which is characterized for each set of experiments in this chapter. Chapter 4 concludes the thesis and discusses the future work beyond this thesis.

2. DC NEGATIVE CORONA DISCHARGES

We discuss the characteristics of negative corona discharges in air and fluid vapors in a pin-to-plate electrode configuration in this section. Here, we provide electrical and spatial characterization for various plate electrodes (anode): solids as well as liquids. Few experiments are also performed at sub-atmospheric pressure with solid anodes. Experiments at sub-atmospheric pressures were performed in a custom vacuum chamber. Solid anodes are chosen to span varying roughness and materials. Liquid anodes are chosen based on polarity and conductivity of the liquids.

2.1. Experimental Setup and Methods

2.1.1. External Circuit

Figure 2.1 shows the schematic of the electrical circuit used to generate DC negative corona discharges. A negative polarity DC power source (Spellman, SL-150) was connected in series with a ballast resistor, the discharge gap (DG) and a shunt resistor. The discharges were produced in pin-to-plate electrode configuration. The pin electrode (tungsten, picoprobe, ST-20-0.5) was connected to the negative polarity power source while the plate electrode (solid or liquid) was connected to ground side of the setup. The DC power source is able to supply upto 3 mA of current and 50 kV (negative polarity) of voltage. A voltage probe (Northstar, PVM-4, input R/C: 400/8 MΩ/pF) was used measure the voltage provided by the DC power source. A current probe (Pearson Electronics, 6585) was connected to the ground (plate) side of the DG. The current probe was used to monitor oscillations of the current in the circuit. An oscilloscope (Tektronix, MSO44) was used to

capture data from both voltage and current probes. A shunt (1 kΩ) was connected in series between ground and the plate electrode. The plate electrode was mounted on a 3-dimensional positioning system. The voltage drop across shunt was measured using a multimeter (Keysight, 34972A). A ballast resistor of 50 MΩ was used for all experiments. All instruments were connected to a computer and data was acquired using LabVIEW [67]. It was observed that the resistance of ballast and shunt changed (<1%) after few sets of experiments and hence the resistance of both the resistors was measured before each experiment to be included in calculations.

The discharge current (I_d) and discharge voltage (V_d) were calculated using the following equations:

$$I_d = \frac{V_s}{R_s} \tag{2.1}$$

$$V_d = V_{DC} - I_d \cdot R_b - V_s \tag{2.2}$$

Here, V_s is the voltage drop across shunt resistor (R_s), V_{DC} is the voltage supplied by the power source (as measured by the voltage probe) and R_b is the resistance of ballast.

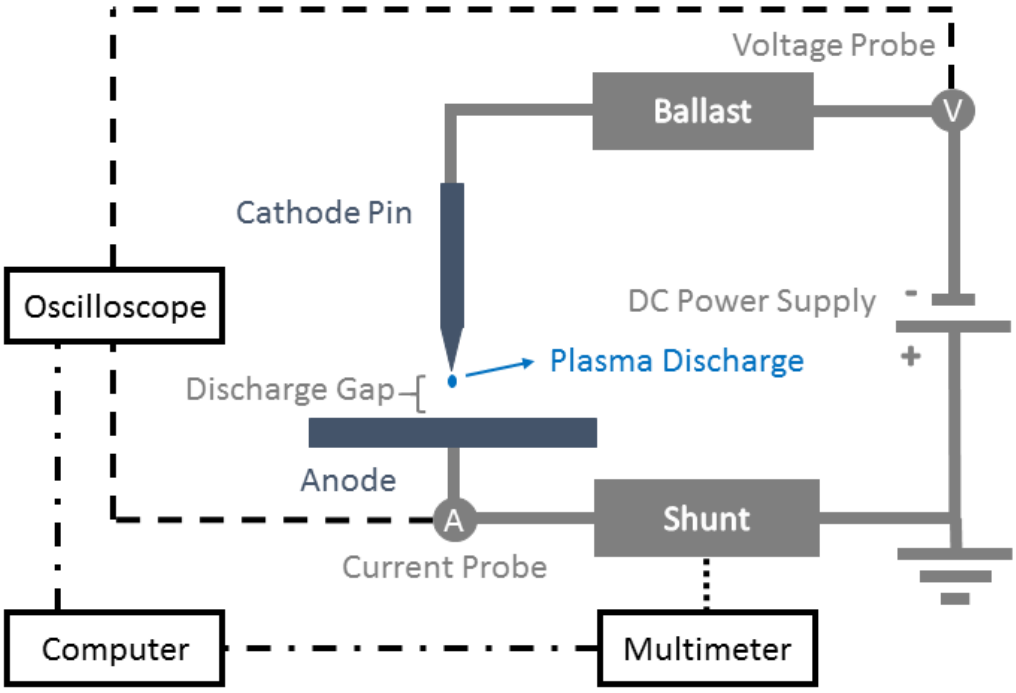

Figure 2.1 External circuit used to characterize the DC negative corona discharge. The thick solid lines represents the connections in the circuit. Dashed line are the BNC cables connecting the voltage and current probe to the oscilloscope. Dotted lines depict the connection across shunt to the millimeter. The oscilloscope and multimeter are connected to a computer as shown using dash-dotted lines.

The study of corona discharges included visualization of discharge, and the characterization of the voltage-current (V-I) characteristics and characterization of anode surfaces. The images and videos were captured using a DSLR camera (Canon EOS 80D) and a high speed camera (Fastcam Nova S9). Both cameras were equipped with either a standard (Canon EFD 18-135 mm)) or a macro lens (Canon MP-E 65mm). All images of discharges were captured in a dark room. Anode surfaces were analyzed under the microscope (Nikon Eclipse LV150N) equipped with a camera (Nikon DS-Fi3) to capture images.

2.1.2. Vacuum Chamber

Plasma discharges at sub-atmospheric pressure were performed inside a custom-made vacuum chamber (Figure 2.2). This also equipped us to do experiments in pure vapor environments with controlled quantity of gas mixtures. We were able to control the amount of non-condensable gases in the chamber and this enabled capabilities to perform experiments with completely and partially degassed liquids. The chamber was assembled by connecting a 6-way cube (Kurt J. Lesker, 2.75”UHV) and a 6-way cross (1.5” Tube OD 2-3/4”CF). All the ports of cube and cross were mated with ConFlat flanges (Kurt J. Lesker) using metal gaskets. Metal gaskets were chosen over the elastomer o-ring, since elastomers may react with a few of the liquids and contaminate the chamber.

Two quartz viewports (Kurt J. Lesker, windows material: corning HPFS 7980 Fused Silica) were attached to the cube for imaging the discharges. The quartz viewports allow the transmission of ultraviolet wavelengths of light. A ball valve to drain liquid and a thermocouple probe to measure liquid temperature were mounted at the bottom of the cube. The remaining two opposite ports on the cube were equipped with a high voltage feedthrough and a ground electrode. These two ports connected the vacuum chamber to the external circuit. Here, the high voltage feedthrough connected the cathode to the negative polarity DC power source and the anode was connected to the ground using a custom-made electrical feedthrough. The discharges are produced in pin to plate electrode configuration. As shown in Figure 2.2, the end of the high voltage feedthrough is connected to a pin electrode (tungsten, picoprobe, ST-20-0.5). Both the high voltage

feedthrough and the ground electrode were electrically insulated with Macor to prevent electrical current leakage to the chamber.

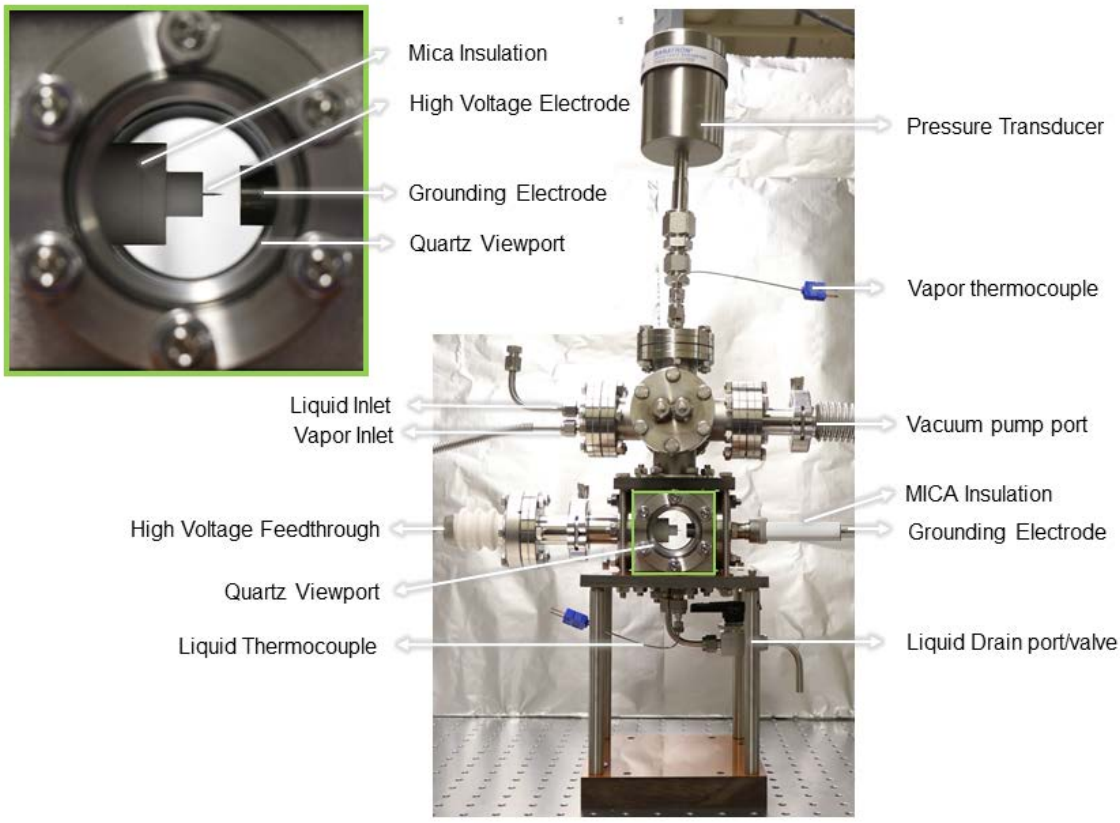

Figure 2.2 Vacuum chamber for plasma discharge. The chamber is equipped with quartz viewports, electrically insulated high voltage and ground electrodes, thermocouples for temperature measurement of liquids and vapors, liquid and vapor inlet ports, and a pressure transducer.

A pressure transducer (MKS Instruments, Baraton Pressure Transducer, 628F13TBE2B) for pressure measurement of the chamber along with a thermocouple probe for temperature measurement of the vapor were connected at the top of the cross. A port of the cross was equipped with a butterfly valve (Kurt J. Lesker) and was connected

to a vacuum pump used to create vacuum conditions in the chamber. The chamber also had ports for liquid and vapor input.

The vacuum chamber was leak tested using a helium leak detector (Pfeiffer Vacuum ASM 340) with leakage rates less than 5×10^{-13} $Pa \cdot m^3 \cdot s^{-1}$. The leakage rate is defined as pressure rise over time in a given volume. The chamber was also tested for electrical isolation from the external circuit.

2.2. Electrical and Optical Characterization of Solid and Liquid Anodes at Atmospheric Pressure

The characteristics of negative corona discharges in air on various solid and liquid anodes is presented here. We study the effect of the interaction of the plasma with:

1. Solid anode surfaces of different roughness
2. Solid anode surfaces of different materials
3. Polarity and conductivity of liquid anodes

To facilitate this we chose two sets of solid anodes, one with varying surface roughness, and the second with smooth (< 5 nm roughness) thin metal films of different thickness and materials deposited on polished silicon wafers. All the cases for solid anode are summarized below in Table 2.1 and Table 2.2 We also selected a set of liquid anodes as listed in Table 2.3.

Table 2.1 Cases studied for solid anode with varying surface roughness (rough anodes).

Case Number	Anode Material	Polishing Materials	Ra [nm]	Rq [nm]
Al1	6061 Aluminum	4000 grit	45	57
Al2	6061 Aluminum	400 grit	475	709
Al3	6061 Aluminum	Emery cloth	5200	6700
Cu1	101 Copper	4000 grit	21	27
Cu2	101 Copper	400 grit	472	602
Cu3	101 Copper	Emery cloth	6400	7300
SS1	316 Stainless Steel	4000 grit	8.5	11
SS2	316 Stainless Steel	400 grit	226	308
SS3	316 Stainless Steel	Emery cloth	1600	2200

Table 2.2 Cases studied for solid anode with thin metal films of metals of different thickness deposited on polished silicon wafers (ultra-smooth anodes).

Case Number	**Deposited Material**	**Thickness [nm]**	**Ra [nm]**	**Rq [nm]**
Si	-	-	0.21	0.31
Al50	Aluminum	50	2.82	3.67
Al100	Aluminum	100	1.79	2.44
Al200	Aluminum	200	4.01	9.38
Cu50	Copper	50	0.9	1.27
Cu100	Copper	100	1.05	1.6
Cu200	Copper	200	1.53	2.22
Ni50	Nickel	50	1.32	1.84
Ni100	Nickel	100	0.9	1.72
Au100	Gold	100	1.24	1.71
Pt100	Platinum	100	3.56	4.49

Table 2.3 Cases studied for liquid anode having different polarity and conductivity [68].

Liquid	Polarity	Conductivity [μS·cm^{-1}]
DI Water	Polar	0.5
Formamide	Polar	10
Silicone Oil (Viscosity: 10cSt)	Non-polar	0
Hexadecane	Non-polar	0

2.2.1. Roughness Measurement

Surface roughness is determined by calculating R_a and R_q. Here, R_a is the arithmetic mean deviation of the assessed profile while R_q is the root mean squared deviation of the assessed profile.

The surface roughness (Figure 2.3) of solid anodes mentioned in Table 2.1 and Table 2.2 was measured using Atomic Force Microscopy (AFM) in the Material Characterization Facility [69] located at Texas A&M University. An AFM (Bruker Dimension Icon AFM) tip radius of 8 nm and the tapping mode was used for these measurements. The scan size for each sample was 60 μm × 60 μm.

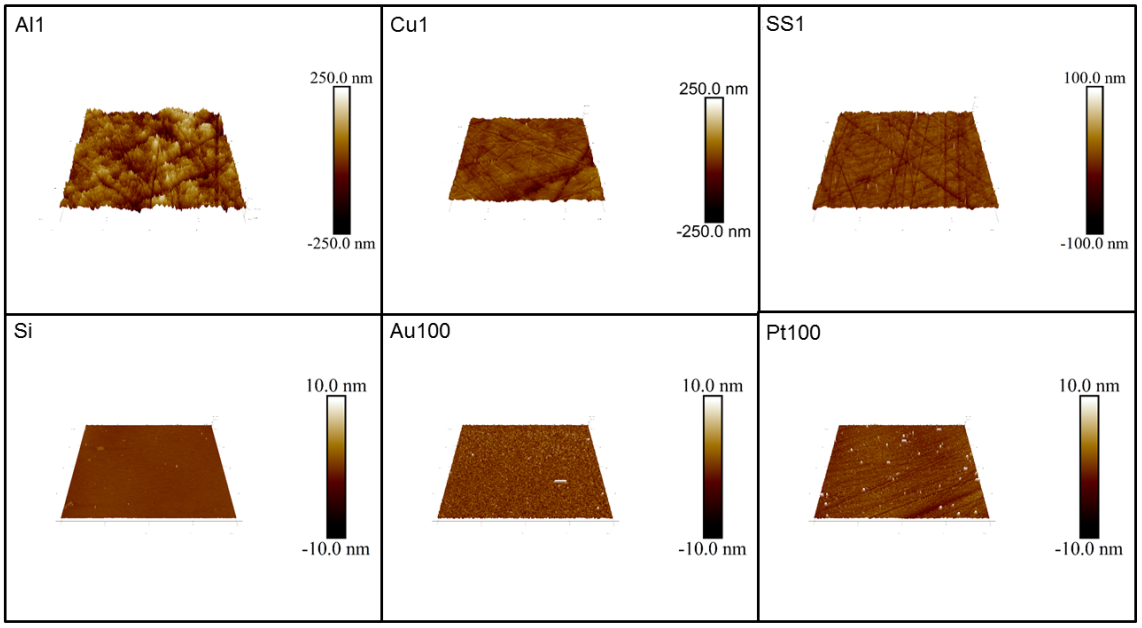

Figure 2.3 Map scan of selected solid anodes listed in Table 2.1 and Table **2.2** obtained from AFM.

Surface roughness measurement of Al3, Cu3 and SS3 samples (Table 2.1) could not be performed with AFM since AFM tips were damaged in each attempt by the substantial surface roughness of these samples. Hence, the surface roughness of these three electrodes was measured using a profilometer (Bruker DektakXT Profiler). The stylus radius was 12.5 μm and a stylus force of 12 mg was used with a scan size of 1 mm × 1 mm.

2.2.2. Anode Electrode Preparation

2.2.2.1. Polishing Plate Electrodes

Three solid anodes were chosen namely 6061 Aluminum, 101 Copper and 316 Stainless Steel. Each of these solid anodes (1” diameter) were polished using P4000 and P400 grit number sandpapers, and, emery cloth providing increasing order of surface

roughness respectively. Solid anodes were sonicated in methanol in a bath sonicator (Crest Ultrasonics P1100D) for 30 minutes to remove the slurry left on the electrode, followed by solvent cleaning with isopropyl alcohol, deionized (DI) water and drying with air before each set of experiments.

The samples were hand polished by keeping sandpaper on a flat piece of glass with solid anode held firmly in hand and moved across sandpaper in upward motion. This was continued till all streaks on the solid anode surface aligned with the direction of sanding. We repeated the process after rotating the solid anode by 90°. This process removed all the scratches greater than the grain size of the sand paper used. The flat glass surface ensured that the electrode surface was flat. For solid anodes polished with P4000 grit number, we started with P400 grit number sand paper and incrementally moved to P4000 grit number using P800, P1200 and P2500 grit number sandpapers in between. The list of electrodes is summarized in Table 2.1 above.

2.2.2.2. Metal Deposition

Thin films of different metals were deposited in the cleanroom of the AggieFab Nanofabrication facility [70] located at Texas A&M University. Single side polished Silicon (Si) wafers (University Wafers) were used for metal deposition with properties mentioned in Table 2.4.

Table 2.4 Properties of purchased single side polished Si wafers.

Type	Dopant	Orientation	Resistivity	Thickness
p	Boron	<100>	1-10 $\Omega \cdot cm$	500 μm

Si wafers were cleaned by immersing in piranha solution containing $3:1$ mixture of 98% H_2SO_4 and 30% H_2O_2 for 10 minutes. A 5 nm adhesion layer of 99.99% titanium (Ti) was deposited followed by 99.99% of aluminum (Al), copper (Cu) or nickel (Ni) using the Kurt J. Lesker PVD 75 Electron-Beam Evaporator (EBE). The wafer was placed in the middle of the substrate holder and rotated at 20 revolutions per minute during deposition to promote film thickness uniformity across the wafer. EBE characteristics are summarized in Table 2.5.

Table 2.5 Electron-Beam Evaporator characteristics.

Parameter	**Value**
Deposition Pressure	5 x 10^{-6} Torr
Deposition rate	1 nm/s
Accelerating voltage	10 kV
Crystal Thickness monitor life	>90%
Substrate rotation speed	20 RPM

Pre-deposited 99.999% gold (Au) and 99.999% platinum (Pt) coated Si wafers were purchased (Platypus Technologies) with properties of the Si wafer similar to those listed in Table 2.4 with thickness of 525 μm and Resistivity of 1-20 Ω·cm. These purchased pre-deposited metal film wafers also had a 5 nm Ti adhesion layer.

The Si wafers were either diced using a dicing saw (Assembly Technologies Micro Automation 100 Dicing Saw) or scribed using a diamond pen into 17 mm × 17 mm. They were then solvent cleaned by methanol, iso-propyl alcohol, water and air dried; in that order before experiments.

2.2.2.3. Liquid Anode

All chemical used for the thesis were purchased from Sigma Aldrich. Water (HPCL Plus, 34877), formamide (ACS reagent ≥99.5%, 47670), hexadecane (ReagentPlus® 99%, H6703) and silicon oil (viscosity: 10 cSt, 378321) were used as liquid anodes (Table 2.3). A quartz cell (Ramé-Hart Instrument Corporation) which was used as liquid container was solvent cleaned by acetone (ACS reagent ≥99.5%, 173124), methanol (ACS reagent ≥99.5%, 179337), iso-propyl alcohol (ACS reagent ≥99.5%, 190764) and water (HPCL Plus, 34877), and, air dried; in that order before the experiments. The dried quartz cell was rinsed twice with the liquid used as the anode. The quartz cell was filled with a liquid and wire was inserted into the liquid and grounded through a shunt resistor. Here, liquid-air interface is the anode surface.

2.2.3. Electrical and Optical Characterization of Solid Anodes

Figure 2.4 and Figure 2.5 show the V-I characteristics of the discharges for the anode surfaces listed in Table 2.1 and Table 2.2 respectively. V-I characteristics for all

cases are presented for three electrode spacings or DGs, *i*.e. 2 mm, 4 mm and 6 mm. The I_d was varied by changing V_{DC}. The observed discharge can be nominally broken down into three regimes with increasing I_d: (1) the negative corona discharge (NCD, blue shaded region) which transitions to (2) the streamer-spark discharge (S-SD, red shaded region) followed by (3) a non-stationary filamentary glow discharge (N-SFGD, green shaded region).

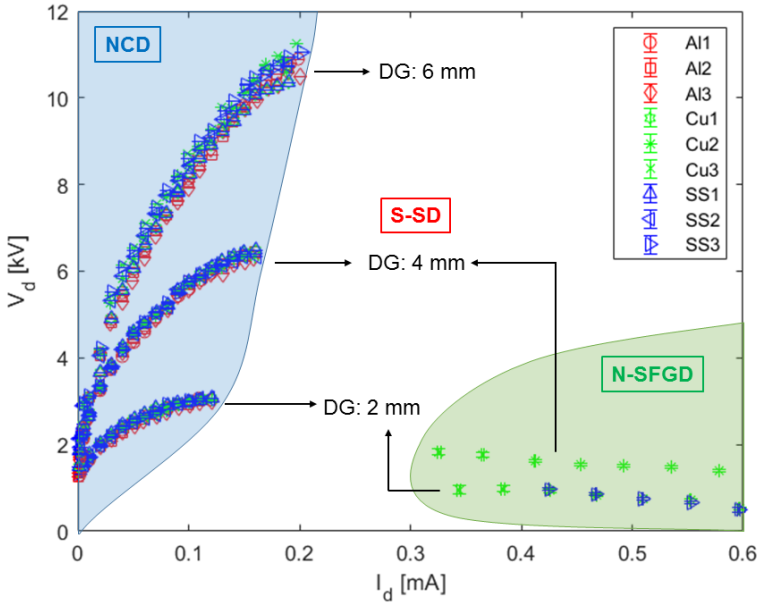

Figure 2.4 V-I characteristics of negative corona discharge (blue shaded region) and non-stationary filamentary glow discharge (green shaded region) for cases listed in Table 2.1.

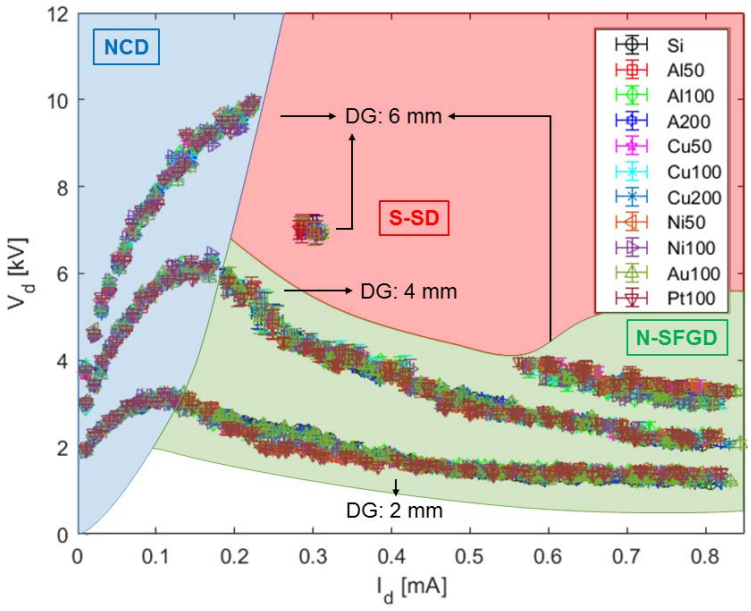

Figure 2.5 V-I characteristics of negative corona discharge (blue shaded region), streamer-spark discharge (red shaded region) and non-stationary filamentary glow discharge (green shaded region) for cases listed in Table **2.2**.

The blue shaded region in Figure 2.4 and Figure 2.5 represents the V-I characteristics of DC NCD regime. Figure 2.6 shows the images of DC NCDs on Au100 for DGs of 2 mm, 4 mm and 6 mm for different I_d values. As can be seen in the Figure 2.6 at lower I_d luminosity of the NCD is concentrated at the pin electrode with the DG being dark. As the I_d is increased, more features are seen in discharge and it can be split into three regions, the luminous corona spot at the tip of the cathode, the diffuse glow near the anode surface which extends into the DG in a conical shape and a dark region in between cathode and anode. The diffuse glow grows brighter as the I_d is increased and brightest before the onset of the S-SD regime. Oscilloscope traces from the current probe indicated that I_d was constant with no AC components other than noise in this regime.

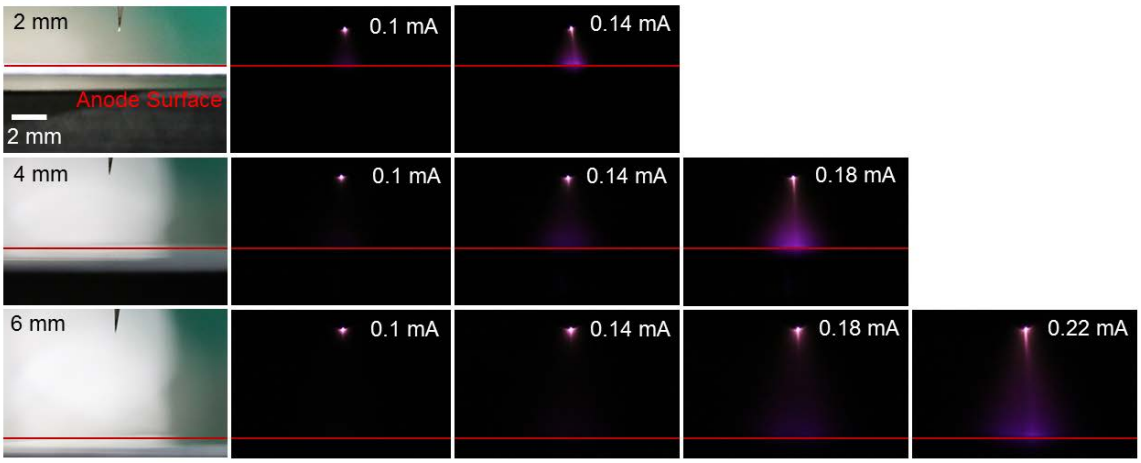

Figure 2.6 Images of DC NCD for Au100 plate electrode at DGs of 2 mm, 4 mm and 6 mm. Exposure time for images is 0.3 s. The negative pin electrode is at the top of the image while solid anode is below.

Constrictions (Figure 2.7a and Figure 2.7b) are also observed along with the diffuse glow in DC NCD regime. These are brighter regions of the discharge (brighter than diffuse glow region but at lower intensity as compared to the corona spot) originating from corona spot at the tip of the cathode and extending to the anode within the diffuse glow region. The constrictions are themselves brightest near the cathode and with decreased brightness closer to the anode surface. They appear to be moving inside the conical shape formed by the diffuse glow in the DG, however, the V_D and I_d are stable (Figure 2.8). Along with the diffuse glow, constrictions grow brighter as the I_d is increased and are brightest before the onset of the S-SD regime. These constrictions are potentially responsible for the structures formed on the anode surfaces (discussed further in Section 2.3).

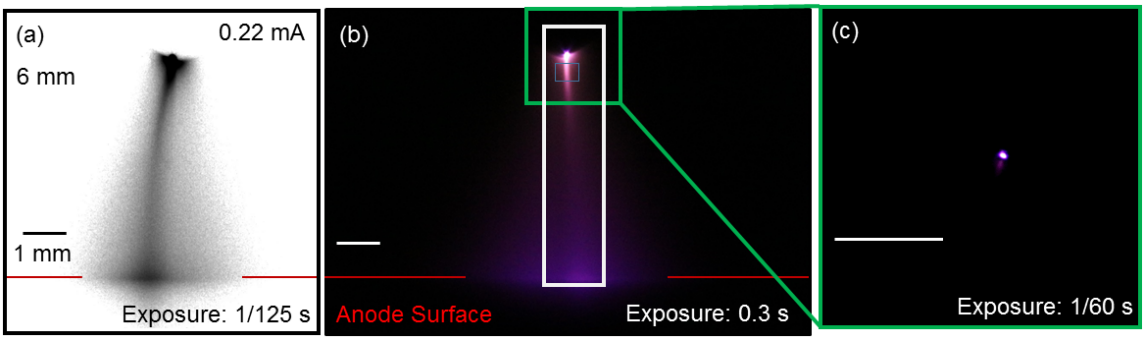

Figure 2.7 (a) False colored image of constriction in DC NCD. The constriction is the dark colored filament within the diffuse glow. Exposure time is 1/125 s. (b) The constriction is encompassed within the white rectangle. Exposure time is 0.3 s. (c) Enlarged image of cathode spot. Exposure time is 1/60 s. Anode is Au100 with DG of 6 mm. The negative pin electrode is at the top of the image and the solid anode is below.

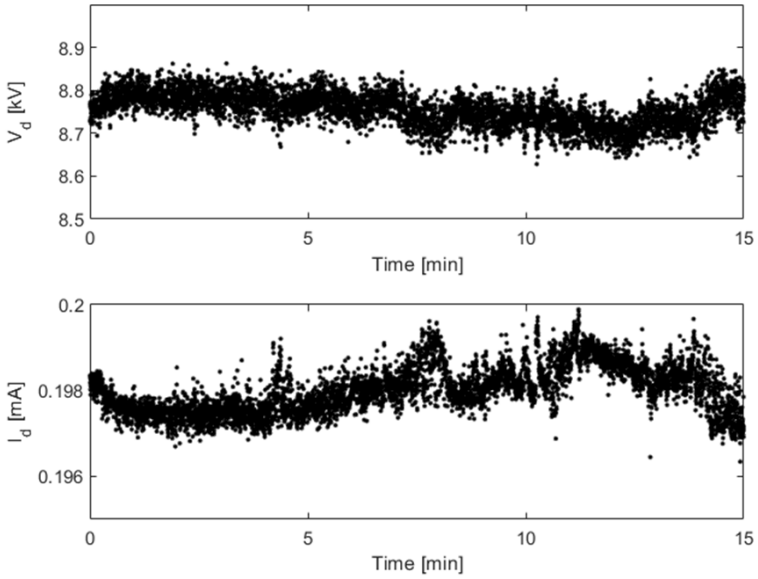

Figure 2.8 Transient V_d and current for solid anode Au100 with DG of 6 mm. The anode is treated for 15 minutes keeping V_{DC} constant.

The slope of V_d and I_d (dV_d/dI_d) stays positive for DC NCD regime for all types of solid anodes. The slope starts decreasing as the I_d approaches the onset of the S-SD regime. The V-I characteristics of surfaces listed in Table 2.1 behaved similarly in DC

NCD regime. The V-I characteristics were not dependent on the roughness (R_a ranging from 10 nm to 5000 nm) of the plate electrodes or the materials. The I_d at transition from DC NCD to S-SD remained consistent for surfaces listed in Table 2.1 for each DG. The V-I characteristics of surfaces listed in Table 2.2 in the DC NCD regime follow trends similar to that of surfaces listed in Table 2.1, but transitions to the S-SD regime at are larger values of I_d. The transitional I_d is also higher for each DG.

The slope (dV_d/dI_d) is negative for S-SD regime. Transition from DC NCD regime to S-SD regime is accompanied by the suppression of the diffused glow region and the formation of sparks or streamers. For cases where sparks are generated, the current pulses are observed making the multimeter inadequate for measurement of I_d. Instead, the current probe is used to capture these current pulses.

Sparks are generated for solid anodes listed in Table 2.1 for all DGs. The sparks keep transitioning to streamers or both are simultaneously generated for the DG of 2 mm. Digitized waveforms (Figure 2.9) with 31.25 million data points and 50 ms in duration were captured by the voltage and the current probes using the oscilloscope for each instance mentioned in Figure 2.10 and Figure 2.11. A sound was heard with the onset of S-SD regime and the pitch of the sound increased with increasing I_d. This sound is possibly due to shock waves generated by sparks as they originate from cathode and move along the DG to the anode creating a pressure change in the surrounding air. Figure 2.10 summarizes the maximum amplitude of the pulses generated for the solid anodes listed in Table 2.1 and Figure 2.11 summarizes the frequency of sparks produced. The maximum current amplitude and frequency of spark for the duration of 50 ms were consistent with a

standard deviation for frequency being less than 2 Hz in a few cases. The value of maximum current amplitude and frequency of spark was inconsistent for DG of 2 mm as the discharge kept transitioning between streamers to spark and back. There was no observable pattern for this transition leading to larger standard deviation.

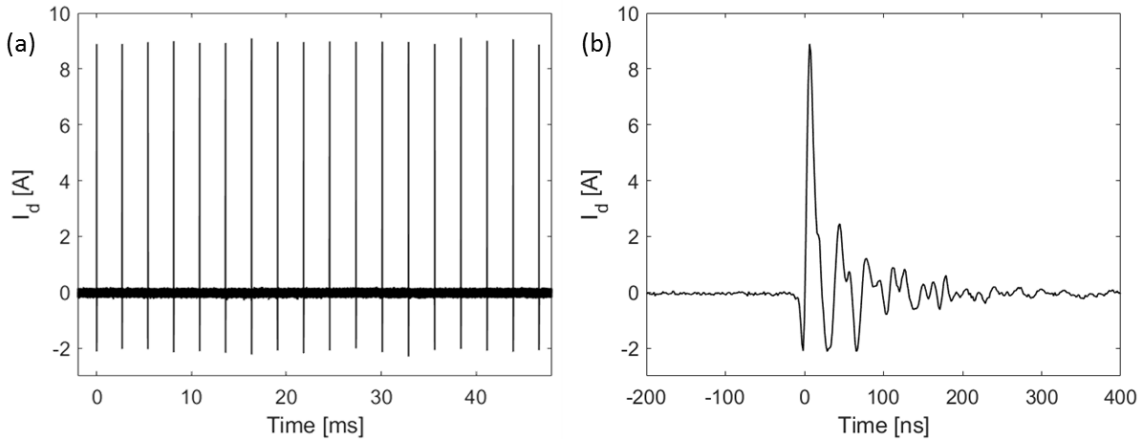

Figure 2.9 (a) Digitized waveform of I_d for SS3 at DG of 6mm and V_{DC} of 20 kV (S-SD regime). (b) Digitized waveform of a single current pulse. Spikes in the waveform represents the spike in I_d due to formation of sparks.

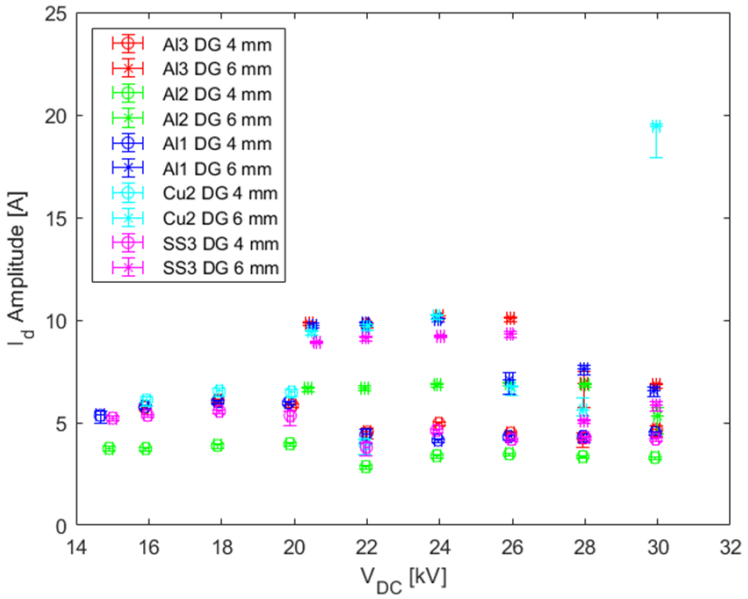

Figure 2.10 Maximum current amplitude of sparks in S-SD regime for the solid anodes listed in Table 2.1.

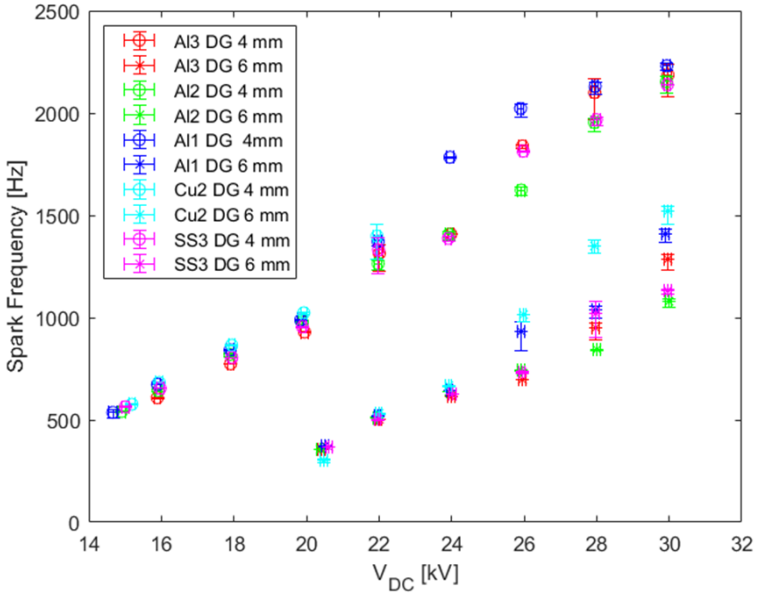

Figure 2.11 Frequency of sparks in S-SD regime for the solid anodes listed in Table 2.1.

For solid anodes listed in Table 2.2, sparks were only observed for DG of 6 mm (Figure 2.12). The observed sparks were accompanied by streamers at the onset of transition S-SD regime but eventually switched to sparks with increasing I_d. For DG of 2 mm (Figure 2.12, 0.2 mA of I_d at DG of 2 mm for Au100) and 4 mm (Figure 2.12, 0.3 mA and 0.4 mA of discharge current at DG of 2 mm for Au100), the NCD directly transitioned to N-SFGD (green shaded region in Figure 2.5). The higher frequency sound could still be heard upon the transition but sparks were not generated. Upon further increase in I_d the higher frequency sound was eventually suppressed. The production of high frequency of sound is indicative of pressure changes in the DG. This pressure change could either be due to movement of N-SFGD across the solid anode surface or generation of current pulses of lower current amplitude, which were not captured by the current probe used. The multimeter worked well for this region and the data captured is presented in of Figure 2.5. It is also possible that the discharge here is generated in the form of low magnitude pulses not captured by the probe used. A solution here would be to measure current pulses with an alternate current probe equipped to measure lower current amplitudes, and imaging of the discharge using a high speed camera. These alternate measurement would possibly identify another regime for such discharges in the V-I characteristics.

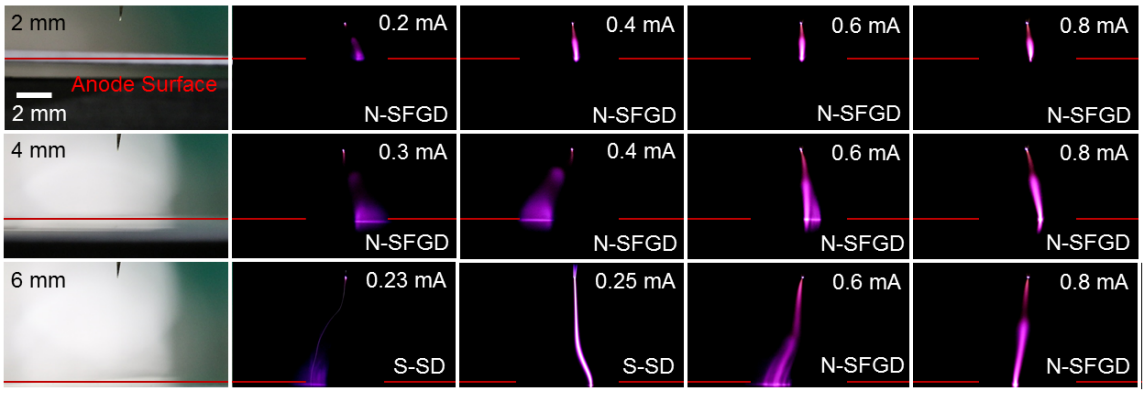

Figure 2.12 Images of S-SD and N-SFGD regime with solid anode Au100 at DGs of 2 mm, 4 mm and 6 mm. Exposure time is 1/60 s. The negative pin electrode is at the top of the image while solid anode is below.

The S-SD transitions to N-SFGD regime upon further increase in I_d (green shaded region in Figure 2.4 and for a DG of 6 mm for Figure 2.5). The high frequency sound is suppressed along with this transition. V_d remains constant in this regime. The transitional I_d for transition from S-SD regime to N-SFGD regime was observed to be inconsistent for solid anodes listed in Table 2.1. The discharges could transition back to S-SD regime even after increasing I_d. This can be attributed to the larger roughness of the anode surface. For solid anodes listed in Table 2.2, the transitional I_d for DG of 6 mm is consistent and the discharges do not transition back to the S-SD regime.

We did not observe consistent, or regular patterns in the movement of the filament in the N-SFGD regime. Although, the movement appears random, high speed camera imaging can be conducted from above (camera lens and anode surface are parallel) to trace the contact point of filament on the anode surface. Alternatively, imaging can also be conducted from below anode surface by depositing thin metal films on glass substrate.

Such anode surfaces would allow light transmission into the camera lens below the anode. This would help identify any patterns resulting from the discharge motion. The rotating filament in glow discharges on solid and liquid anodes [71] as well as other patterns on liquid anodes due to the presence of a filament have been observed by others [72]. The movement/motion of the filament eventually stops at a single point (stationary filamentary glow discharge) on the solid anode surface with increasing I_d. The uncertainty of measured V_d and I_d also decreases as the filament stops at a single point on the solid anode surface. Oscilloscope traces from the current probe indicated that I_d was constant with no AC components other than noise. The I_d at which N-SFGD becomes stationary has been observed to be inconsistent across the experiments for all solid anode surfaces. A detailed study needs to be conducted studying the role of surface roughness and thickness of oxidized film (for the materials being oxidized by discharge) for this transition.

2.2.4. Electrical and Optical Characterization of Liquid Anodes

Figure 2.13 shows the V-I characteristics of the discharge for polar and conductive DI water at three electrode spacings (gap between cathode tip and liquid-vapor interface) or DGs, *i*.e. 2 mm, 4 mm and 6 mm. The I_d was varied by changing the V_{DC}. The observed discharge can be broken down into three regimes with increasing I_d: (1) the NCD (blue shaded region) which transitions to (2) a transitional regime (TR) followed by (3) the N-SFGD regime (green shaded region).

Similar to solid anodes, in the NCD regime at lower I_d the NCD is concentrated at the pin electrode with DG being dark (Figure 2.14). As I_d is increased a diffuse glow near the surfaces appears which extends into the DG in a conical shape. Upon further increase

in I_d, similar to a solid anode, the discharge transitions into the N-SFGD regime. The filament in the N-SFGD is broadened into a conical shape closer to the anode (Figure 2.14). Similar conical shapes has been observed for DI water for spark discharges at larger I_d [72]. This broadening of the filament decreases with increasing conductivity of water as the charge carrier density in liquid becomes higher requiring smaller contact area. Figure 2.13 shows the V-I characteristics for few sets of experiments with water where I_d is increased to 0.8 mA and is decreased to 0 (to test for hysteresis, explained below). The DG is measured after each cycle of such experiment and was observed to increase by ≈100 μm. This change in DG is due evaporation of water. The slight differences in the V-I characteristics for increasing and decreasing the current can be attributed to this change in DG. We did not monitor the changes in the conductivity of water over time and this may have a potential effect too.

For DG of 2 mm both negative corona discharge regime and non-stationary filamentary corona discharge regime can be observed for a range of values of I_d. While increasing the I_d, the transition from NCD to N-SFGD is at higher current value compared to when current is decreased (transition from N-SFGD). This hysteresis effect is only observed for DG of 2 mm. A transitional regime (TR) is also observed when decreasing the I_d for DG of 6 mm where the discharge keeps switching in between the NCD and the N-SFGD. This is not observed when increasing the I_d for DG of 2 mm or for DG of 4 mm and 6 mm.

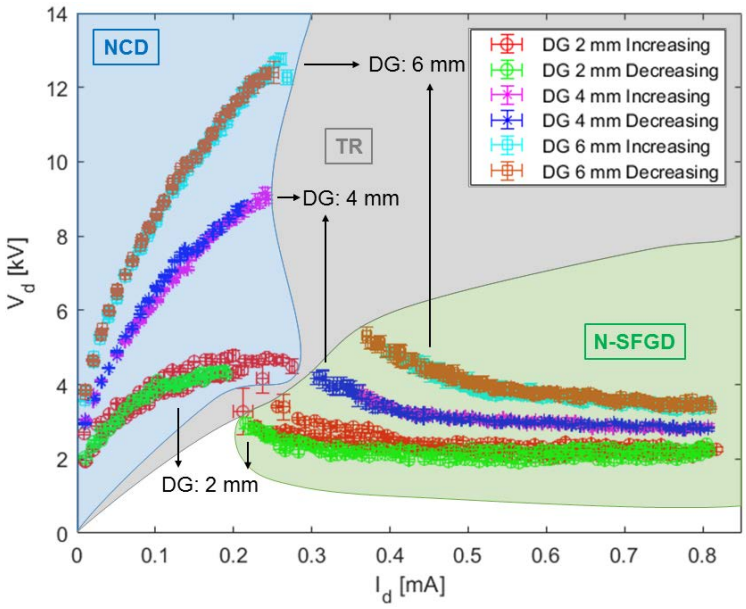

Figure 2.13 V-I characteristics of NCD (blue shaded region), NCD to N-SFGD transitional regime (grey shaded region) and N-SFGD (green shaded region) for water. Multiple experimental results are being plotted for all DGs.

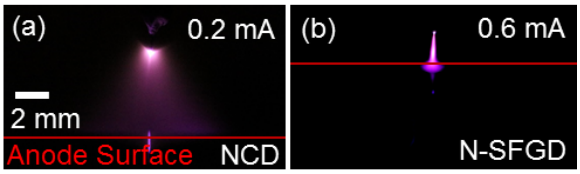

Figure 2.14 Images of (a) DC NCD (DG of 6mm, exposure time 1 s) and (b) N-SFGD (DG of 2mm, exposure time 1/60 s) above DI water as liquid anode. The negative pin electrode is at the top of the image while liquid anode is below.

A concave meniscus (dashed red line, Figure 2.15) is observed under the cathode in the NCD regime for water. The interface of meniscus stays unstable and the size of the meniscus increases with increasing I_d. This concavity can be attributed to the combination of the corona wind (air and ion flow induced by electrostatic forces [73] and surface charge [74]. The concavity in meniscus diminishes to smaller radius/area with the transition to

the N-SFGD regime. Further studies can be conducted to calculate the curvature of the meniscus assuming that it is axisymmetric. Estimation of pressure exerted by discharge (P) on anode surface can be made using the following relation:

$$P = 2 \cdot \gamma \cdot K \qquad 2.3$$

Here, γ is the surface tension of water and K is the mean curvature of the meniscus.

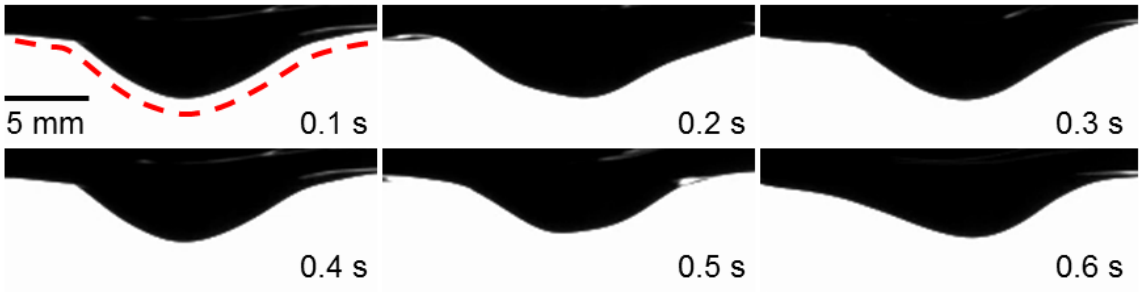

Figure 2.15 Concave meniscus of water (dashed red line) under the cathode at I_d = 0.26 mA and DG of 6 mm in NCD regime. The images shows changing meniscus shape with time. Exposure time for images is 1/1000 s. The liquid-vapor interface is at the top of the image.

Figure 2.16 shows the V-I characteristics of the discharge for another polar and conductive fluid formamide for DGs, of 2 mm, 4 mm and 6 mm. Similar to water, experiments were conducted by increasing the I_d to 0.8 mA followed by decreasing it to 0 mA. No observable change in DG was observed for formamide since its boiling point at 1 atm is 210 °C, which is 110 °C higher than the boiling point of water at 1 atm (100 °C). The observed discharge is similar to water and can be broken down into similar regimes (Figure 2.17). The hysteresis effect was not observed for formamide. Instead, formamide has a comparatively larger TR where the discharge switches between the NCD and the N-

SFGD. This also leads to fluctuations in I_d and it is the reason for larger uncertainty bars in this region. Rapid movement of the filament in the N-SFGD regime over the anode surface were observed (Figure 2.17b). A concavity in meniscus similar to water was also observed in the NCD regime (Figure 2.17c).

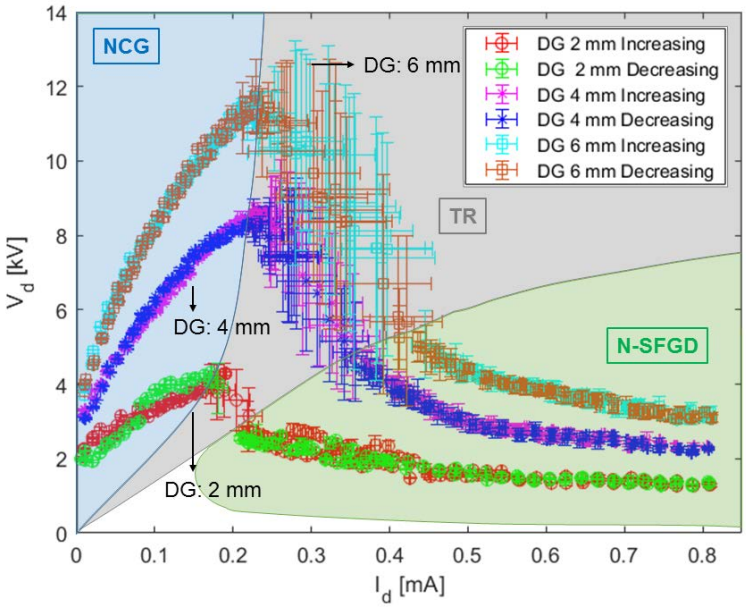

Figure 2.16 V-I characteristics of NCD (blue shaded region), NCD to N-SFGD transitional regime (grey shaded region) and N-SFGD (green shaded region) for formamide.

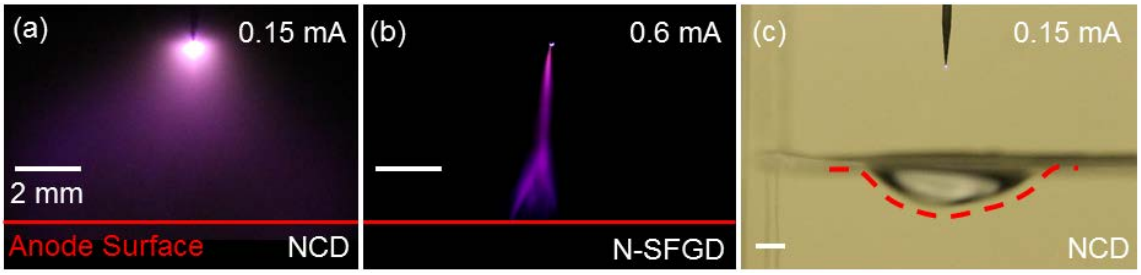

Figure 2.17 Images of (a) DC NCD (exposure time 1 s) and (b) N-SFGD (exposure time 1/60 s) above formamide as the liquid anode, and, (c) concave meniscus of formamide (dashed red line, exposure time 1/60 s) under the cathode at DG of 6 mm. The negative pin electrode is at the top of the image and the liquid anode is below.

Figure 2.18 shows the V-I characteristics of the discharge for hexadecane for DGs of 2 mm, 4 mm and 6 mm. Unlike water and formamide only the NCD is observed (Figure 2.18). The DG stays dark with increasing I_d without appearance of the diffuse glow and discharge never transitions to the N-SFGD. A smaller (compared to water and formamide) concavity in the meniscus is also observed. Silicone oil and hexadecane are fluids with low electrical conductivity, leading to low I_d (compared to water and formamide). The V-I characteristics (Figure 2.18) for each fluid are independent of the DG. Although, silicone oil has lower V_d for same value of I_d when compared to hexadecane. Si-O bonds are polar due to difference in the electronegativity of Si and O, but in silicone oil, the presence of long chain suppresses its polarity. In NCDs, presence of electric field could result in some dipole moment in silicone oil, making them more conductive compared to hexadecane.

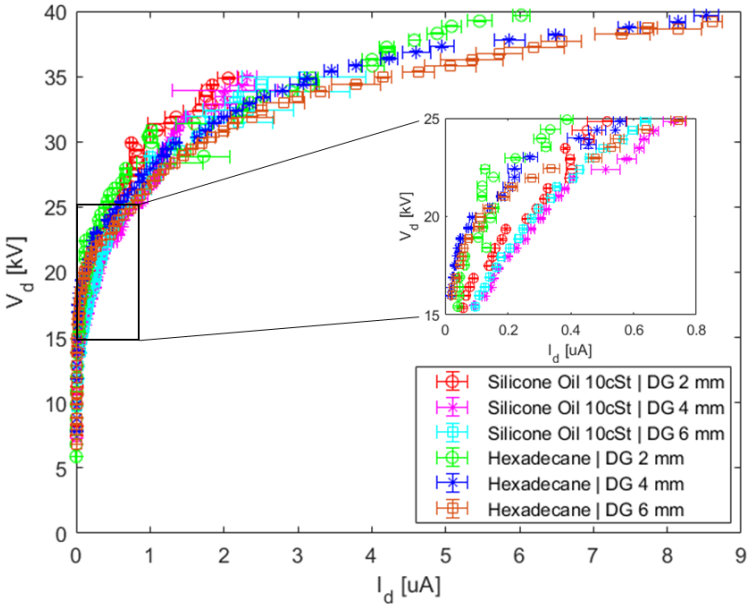

Figure 2.18 V-I characteristics of DC NCD above silicone oil and hexadecane.

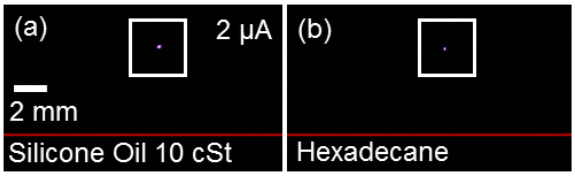

Figure 2.19 Images of DC NCD above (a) silicon oil and (b) hexadecane as liquid anode at DG of 6 mm. The exposure time is 1 s. The negative pin electrode is at the top of the image while liquid anode is below.

2.3. Surface Characterization of Solid Anodes

Here, we characterize the surface of solid anodes (Table 2.1 and Table 2.2) treated with plasma discharges using roughness measurements (AFM and profilometer), wetting tests, adhesion tests and X-ray photoelectron spectroscopy (XPS). Solid anode surfaces were treated in the NCD regime with a constant I_d = 0.18 mA for 30 minutes at DG of 6 mm. The NCD operated with a diffuse glow for this combination of I_d and DG.

2.3.1. Optical Characterization

Visible changes were observed in surface texture for all solid anode surfaces. Anode surfaces were analyzed under the microscope (Nikon Eclipse LV150N) equipped with a camera (Nikon DS-Fi3) to capture images. The surface seems to be most affected directly beneath the cathode with diminishing effects towards the edge of the anode surface under the diffuse glow. The anodes listed in Table 2.1 had a dark center surrounded by a dull ring (Figure 2.20d - Figure 2.20f).

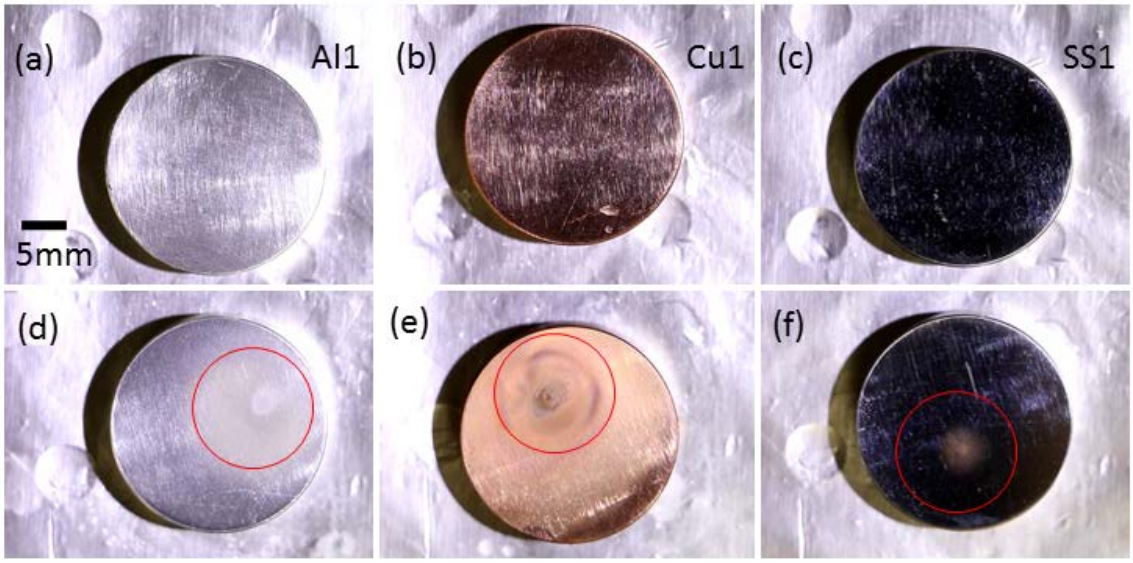

Figure 2.20 Images of Al1, Cu1 and SS1 (a-c) before and (d-f) after discharging with a constant I_d = 0.18 mA for 30 minutes at DG of 6 mm. Anodes were treated with cathode at the top of the center of the red circle (d-f). (d-f) had a dark center surrounded by a dull surface compared to (a-c).

Al200, Cu200 and Ni100 had a darker center similar to anodes listed in Table 2.1 (Figure 2.21a - 2.21c). This darker center appears to be either of the exposed Ti adhesion

layer or the Si (or Ti oxide) substrate. The discharge likely oxidizes the anode surface and the metal oxides potentially have poor adhesion to the solid anode, leaving the Ti adhesion layer or Si substrate exposed at the center. The color of the treated anode surfaces closer to the edges of diffuse glow appears similar to untreated samples, indicating that the thin metals films are still intact. Several surface patterns are observed in the center region of all anode surfaces (Figure 2.21).

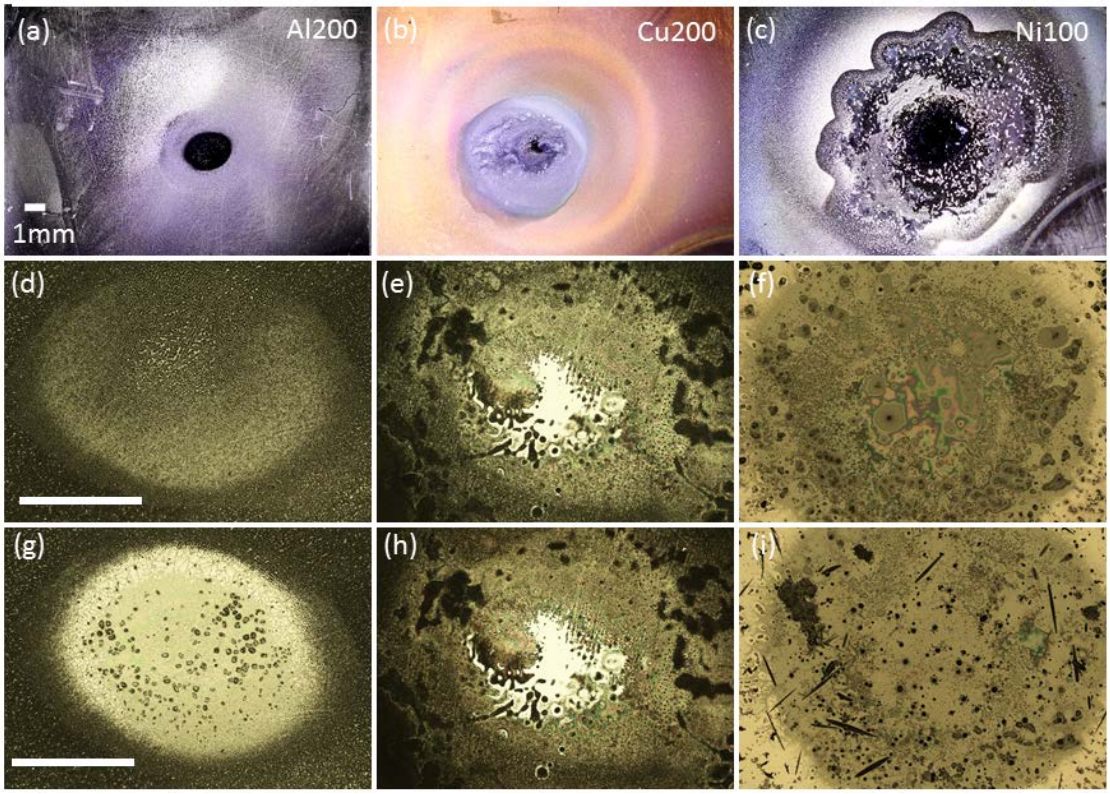

Figure 2.21 Images of Al200, Cu200 and Ni100 treated with a constant I_d = 0.18 mA for 30 minutes at DG of 6 mm. Images of anodes (a-f) before and (g-i) after treating with Ar plasma for 90 minutes. Scale bar is 1 mm for all images.

For Au100 and Pt100 no damage was observed to the deposited metal layer. Instead, microscopic structures were observed on the surface (Figure 2.21d - 2.21f). Similar structures were observed for Si (Figure 2.21d). These structures have higher density at the center and the density decreases closer to the edge of the anode surface. Compared to Si and Au100, the surface of Pt100 under the diffuse glow was less effected by the discharge. In the following sections we will analyze these structures further.

Table 2.6 Melting point and oxidation potential for half reactions of metals used for thin film deposition on Si substrate in Table **2.2**.

Material	**Melting Point [°C] [75]**	**Half Reaction**	**Standard Oxidation Potential [V] [75]**
Al	660	$Al \rightarrow Al^{3+} + 3e^{-}$	1.662
Ni	1455	$Ni \rightarrow Ni^{2+} + 2e^{-}$	0.23
Fe	1538	$Fe \rightarrow Fe^{2+} + 2e^{-}$ $Fe \rightarrow Fe^{3+} + 3e^{-}$	0.44 0.04
Cu	1085	$Cu \rightarrow Cu^{2+} + 2e^{-}$ $Cu \rightarrow Cu^{+} + e^{-}$	-0.337 -0.520
Pt	1768	$Pt \rightarrow Pt^{2+} + 2e^{-}$	-1.18
Au	1064	$Au \rightarrow Au^{3+} + 3e^{-}$ $Au \rightarrow Au^{+} + e^{-}$	-1.52 -1.83

Table 2.6 shows the standard oxidation potential of metals. Al, Ni and Cu are more prone to oxidation compared to Au and Pt. We can also confidently state that the materials

on the anode are not melting since the melting point of Cu and Au are similar, but Au films adhere to surface while Cu does not after NCD regime plasma treatment.

2.3.2. Adhesion Testing

In order to determine the nature of structures formed on the solid anodes we performed a few adhesion tests. The purpose of these tests were to probe the structures on the surface: are they oxides chemically bonded to the metal or are they other materials deposited on the anode surface? The surface of the solid anodes was wiped with lint free paper (Kimtech). This wiping action removed the structures from Si, Al100 and Pt100. However Al200, Cu200 and Ni100 were not affected. The wiping process did scratch/damage the surface of these anodes. For the solid anodes listed in Table 2.1 wiping action removed some material from the dark center.

Few anodes were treated in Argon (Ar) plasma using a plasma cleaner (EM clean plasma cleaner, PIE Scientific) mounted on a vacuum chamber. The plasma cleaner operated at a pressure of 100 mTorr and power of 75 W. The density of structures on surface of Si, Au100 and Pt100 was reduced after 10 minutes of treatment (Figure 2.22). The anodes were treated in Ar plasma for 90 minutes, however, most changes were observed after the first 10 minutes of treatment. Only minor changes in structures at the center of Al200 and Ni200 (Figure 2.21) were observed. Similar to the case of Si, Au100 and Pt100, these changes were observed after 10 minutes of Ar plasma treatment and further treatment did not result in major visible structural changes on the anode surface. The color of Cu200 anode became darker after Ar plasma treatment indicating that Ar

plasma was slowly removing the thin film of Cu exposing the Si wafer underneath it. No changes were observed for SS1 after 90 minutes of Ar plasma treatment (Figure 2.23a).

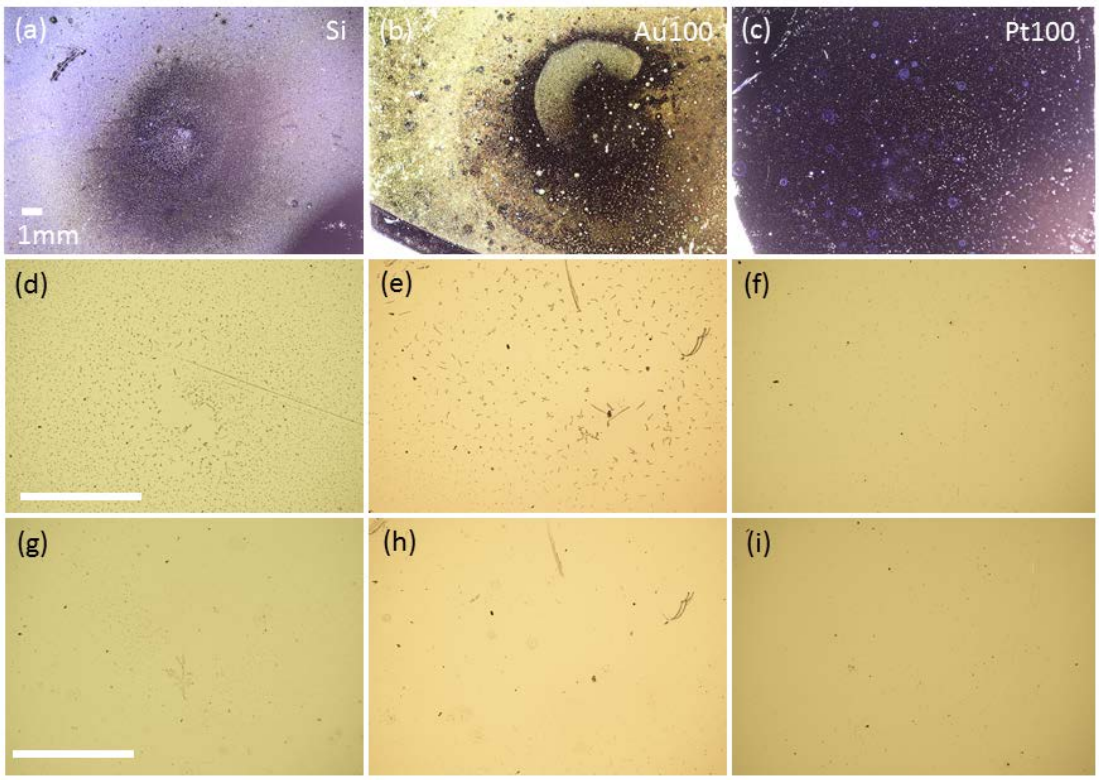

Figure 2.22 Images of Si, Au100 and Pt100 treated with a constant I_d = 0.18 mA for 30 minutes at DG of 6 mm. Images of anodes (a-f) before and (g-i) after treating with Ar plasma for 90 minutes. Scale bar is 1 mm for all images.

ASTM D3359 adhesion rating tape test were also performed on the solid anodes listed in Table 2.1. A lattice pattern with six cuts in each directions was scribed through the dark center spot of the anodes treated with a constant I_d = 0.18 mA for 30 minutes at DG of 6 mm. A pressure sensitive scotch tape was applied over the lattice pattern for 90 seconds and then removed. The adhesion is assessed qualitatively on a scale of 0-to-5. All

anodes were rated 5 with smooth edges of the cuts and without detachment of the material in the lattice. Image of SS1 before applying and after removing the tape is shown in Figure 2.23.

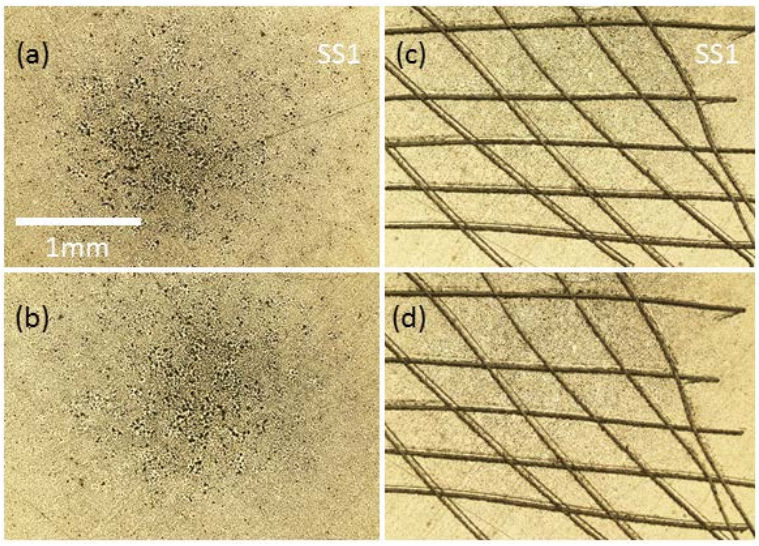

Figure 2.23 Images of SS1 treated with a constant I_d = 0.18 mA for 30 minutes at DG of 6 mm. (a) Images of anodes before and (b) after treating with Ar plasma for 90 minutes. Images of anodes (c) before and (d) after ASTM D3359 adhesion testing.

2.3.3. Wetting Test

A wetting test using DI water was performed on the anodes treated with a constant I_d = 0.18 mA for 30 minutes at DG of 6 mm. A drop of water was placed on discharged and non-discharged anode surfaces for comparison of wettability. The contact angles of water droplets on plasma treated Al1, Cu1, SS1 and anodes listed in Table 2.2 were lower than the untreated anodes. For plasma treated Al2, Al3, Cu2, Cu3, SS2 and SS3 the contact angle was higher than the untreated anodes. The higher contact angle for plasma treated

samples can potentially be attributed to the droplet forming in a Cassie-Baxter state for untreated anode surfaces and in Wenzel state for plasma treated anode surfaces.

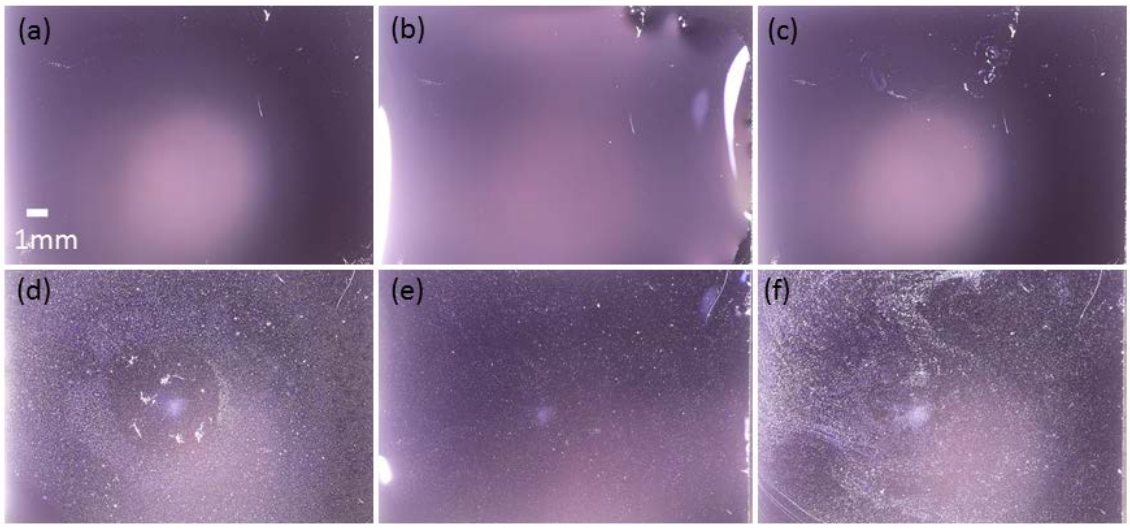

Figure 2.24 (a) Untreated Si before adding the water droplet, (b) after adding water droplet and (c) after evaporation of water from the surface. (d) Plasma treated Si surface before adding the water droplet, (e) after adding water droplet and (f) after evaporation of water from the surface with reorganized structures. Si was treated with a constant I_d = 0.18 mA for 30 minutes at DG of 6 mm. The brighter pinkish spot on the (a)-(c) is the reflection of camera lens, the surface has uniform color.

The water droplet added during the wetting test was able to reorganize structures on Si, Al100 and Pt100. This indicated poor adhesion of the structures on these surfaces formed by the diffuse glow interacting with the anode surface. Figure 2.24d shows plasma treated Si. A water droplet was added on the Si substrate (Figure 2.24e) reorganizing structures on it (Figure 2.24f) after evaporation at ambient temperature. The impurities dissolved in water are not the reason for these structures. This was examined by adding (Figure 2.24b) and evaporating (Figure 2.24c) water on an untreated Si surface. Some

white impurities were deposited on the untreated Si surface after evaporation (Figure 2.24c), however this deposition cannot account for the observations on plasma treated Si (Figure 2.24f). This confirms the poorly adhering structure formation on plasma treated Si.

2.3.4. Surface Roughness Measurements

Surface roughness of few anode surfaces were measured using AFM after treating with NCD at a constant I_d = 0.18 mA for 30 minutes at a DG of 6 mm. The roughness was measured at the center of the anode (the spot under the cathode at the time of the discharge) and at the edges of the region on the anode under the diffuse glow. The surface roughness for all anodes increased after the NCD regime plasma treatment (Table 2.7). The surface roughness of Al200 and Cu200 at the center is less than the surface roughness at the edges. This can potentially be due to either exposed adhesion layer of Ti or the Si substrate itself. Although, surface roughness of Si is known and lesser than both Al200 and Cu, the surface roughness of the thin metal film of Ti (or oxidized Ti) needs to be measured. The surface roughness across the Si and Au100 surface has slight variations when compared to Al200 and Cu200. The size and type of structures formed on Si, Au100 and Pt100 vary by a smaller extent when compared to Cu200, Al200 and Ni100. The center of Cu1 is rougher than the edges. The dark center might have potentially more structures (Figure 2.20e) when compared to the edges of the anode.

Table 2.7 Surface roughness of materials of few untreated and plasma treated anodes listed in Table 2.1 and Table 2.2 measured at the center and edge of the anode. Anodes were plasma treated with a constant I_d = 0.18 mA for 30 minutes at DG of 6 mm.

Case Number	**Untreated**		**Plasma treated with a constant I_d = 0.18 mA for 30 minutes at DG of 6 mm**			
			Center		**Edge**	
	Ra [nm]	**Rq [nm]**	**Ra [nm]**	**Rq [nm]**	**Ra [nm]**	**Rq [nm]**
Si	0.21	0.31	2.9	5.4	2.2	10.4
Al200	4.01	9.38	9.4	11.5	161	328
Cu200	1.53	2.22	5.4	20.2	85.8	102
Au100	1.24	1.71	31	59	9	24
Cu1	21	27	314	416	196	245

2.3.5. X-Ray Photoelectron Spectroscopy Characterization

XPS was used to analyze anodes Au100 and Si to determine the chemical composition of the micro/nano structures formed. Figure 2.25 shows survey spectra of untreated (Figure 2.25a) and plasma treated Au100 (Figure 2.25b). Larger O1s peak in plasma treated Au100 (Figure 2.26a) compared to untreated Au100 (Figure 2.26b) is indicative of metal oxide formation. Si element or silicon oxide peaks were not detected, affirming that thin metal film of Au100 is not damaged during plasma treatment which would expose the Si substrate.

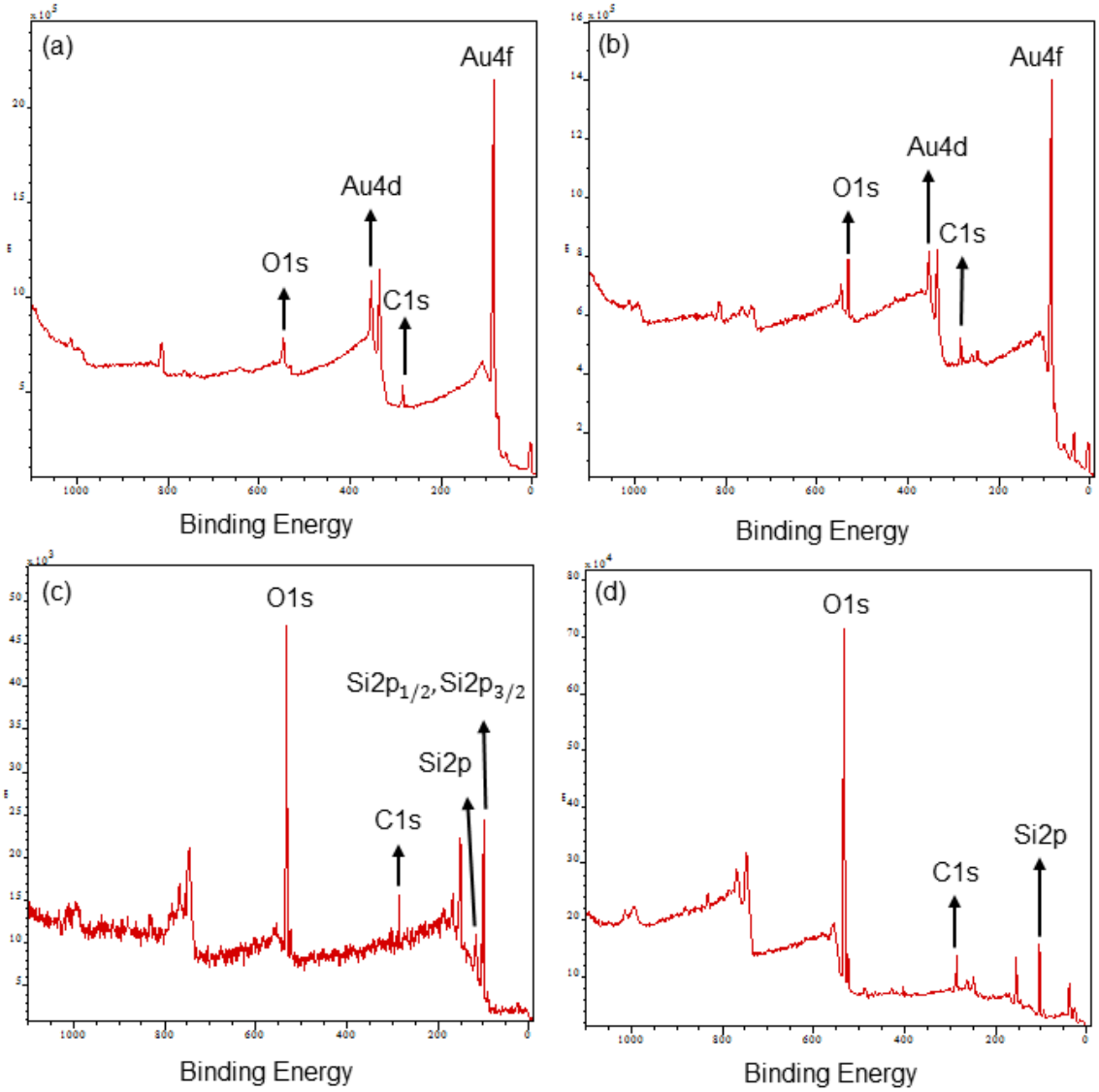

Figure 2.25 Survey spectra of (a) untreated and (b) plasma treated Au100, and, (c) untreated (d) plasma treated Si. Au100 and Si we treated with a constant I_d = 0.18 mA for 30 minutes at DG of 6 mm.

Figure 2.25 shows survey spectra of untreated (Figure 2.25c) and plasma treated Si (Figure 2.25d). Si element (Si2p) and silicon oxide peaks ($Si2p_{1/2}$ and $Si2p_{3/2}$) were detected on untreated Si surface (Figure 2.27c). A strong silicon oxide peak was detected for plasma treated samples (Figure 2.27d) indicating that top of the Si surface is

completely oxidized. This was also confirmed by thickness measurement of SiO_2 on the plasma treated sample using the ellipsometer located in the Material Characterization Facility [69].

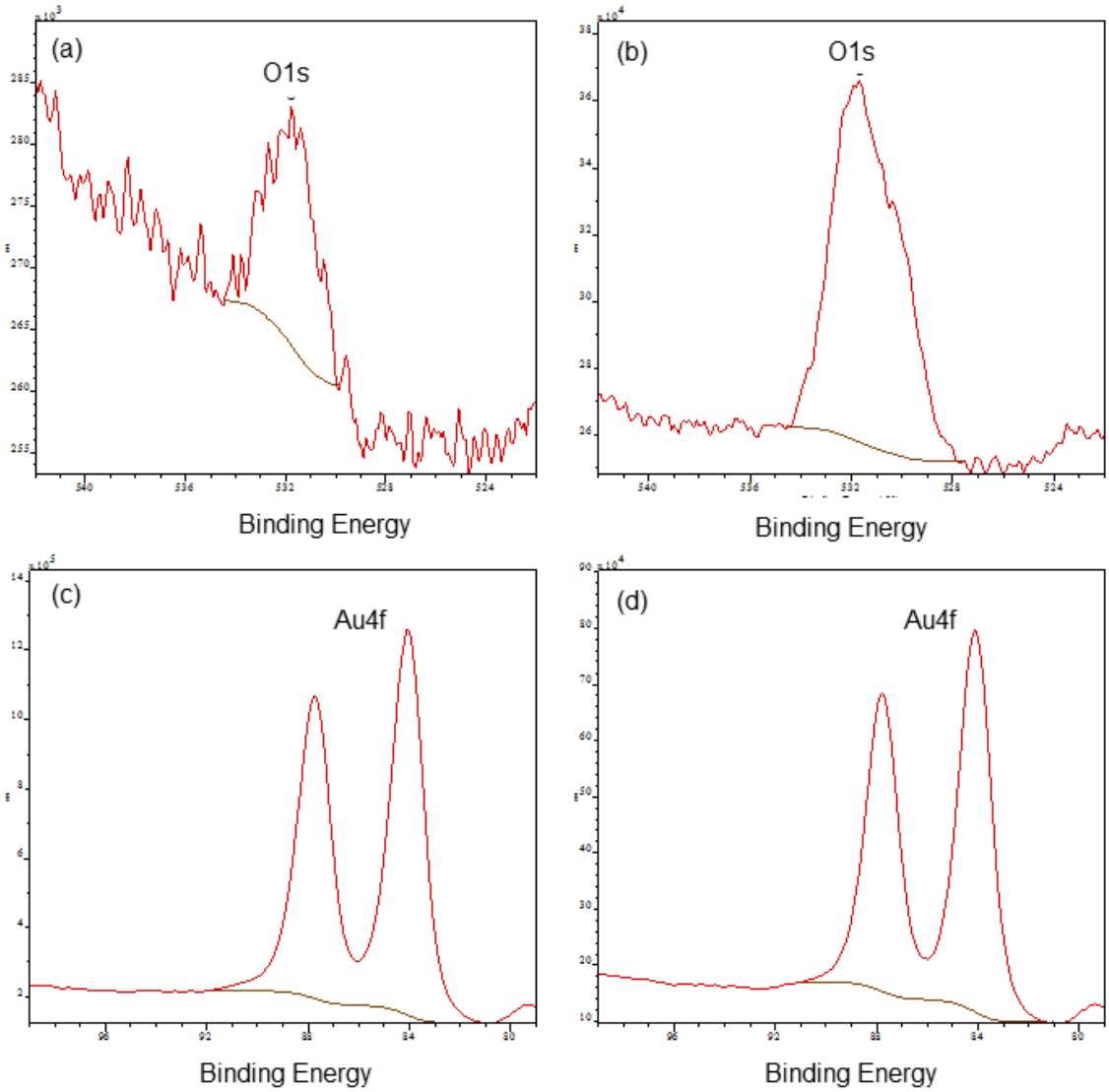

Figure 2.26 Au100 peaks of O1s for (a) untreated (b) plasma treated surface, and, Au4f peaks for (c) untreated and (d) plasma treated surface. Au100 was treated with a constant I_d = 0.18 mA for 30 minutes at DG of 6 mm.

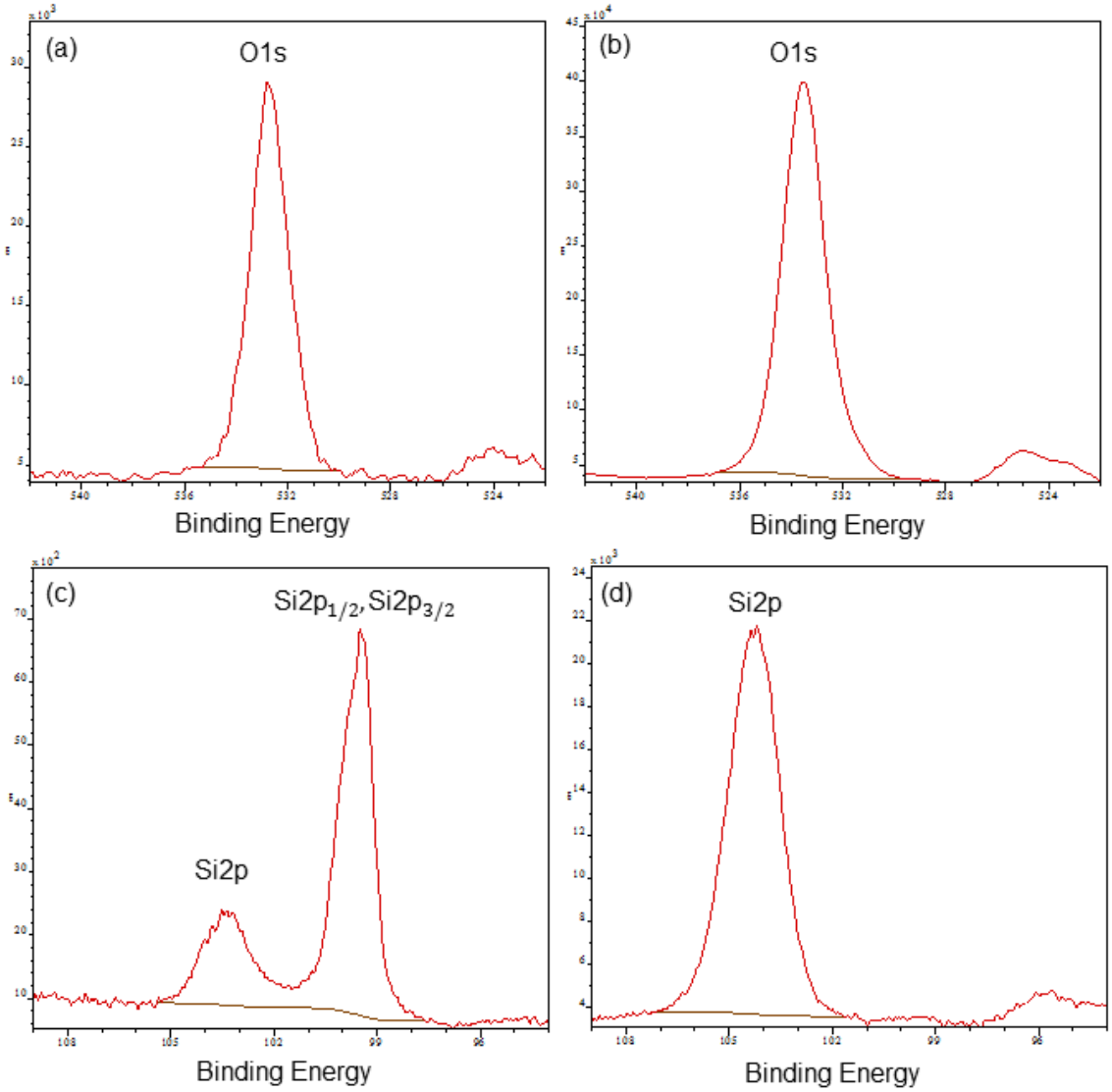

Figure 2.27 Si peaks of O1s for (a) untreated (b) plasma treated surface, and, Si2p peaks for (c) untreated and (d) plasma treated surface. Si was treated with a constant I_d = 0.18 mA for 30 minutes at DG of 6 mm.

SiO_2 thickness for the plasma treated sample was measured as ≈22 nm compared to ≈3 nm for untreated Si. Over 70% of the XPS signal comes from outer 10 nm and over 90% of signal comes from outer 20 nm and this explains the reason for the absence of Si

elemental peak in the post plasma treated XPS signal (Figure 2.27d). The oxygen peaks of untreated (Figure 2.27a) and plasma treated (Figure 2.27b) Si looked identical.

2.3.6. Cathode Characterization

Figure 2.28 shows SEM and microscopic images of unused tungsten pin (cathode) electrode and after few minutes of using it as cathode with a constant constant I_d = 0.18 mA for 30 minutes at DG of 6 mm. As the cathode is used over time, the radius of the tip increases and nano-structures are formed on the tip as can be seen in Figure 2.28 (red box). The nanostructures are potentially formed due to oxidation of tungsten.

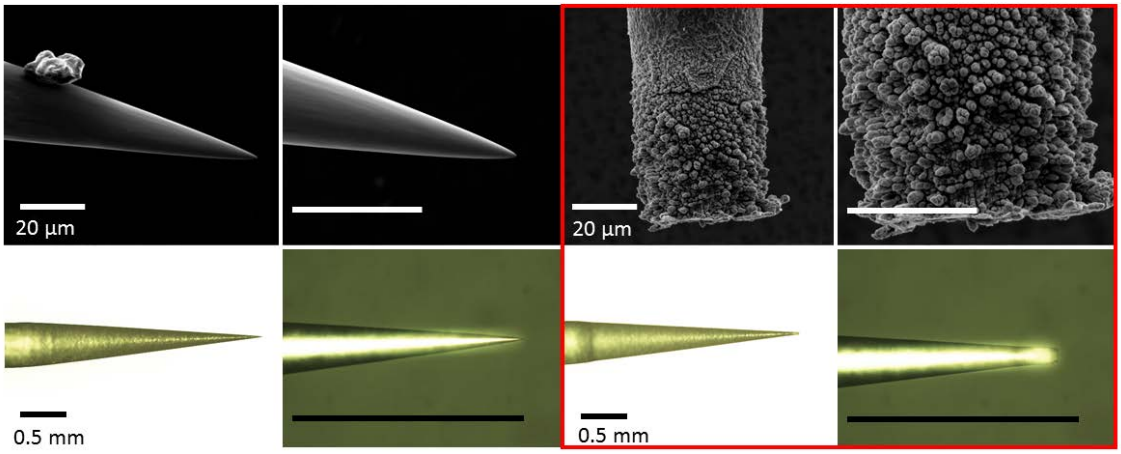

Figure 2.28 Images of tungsten electrode before and after (red box) discharged with a constant I_d = 0.18 mA for 30 minutes at DG of 6 mm

2.4. Electrical and Optical Characterization of Solid Anodes as Sub-Atmospheric Pressure

DC plasma discharge experiments with Cu1 (Table 2.1) were repeated at sub-atmospheric pressure of 1 kPa and 50 kPa in the vacuum chamber (Figure 2.2) for DGs of

2 mm, 4 mm and 6 mm. The circuit depicted in Figure 2.1 was used with cathode and anode connected to the external circuit via the high voltage feedthrough and the ground electrodes. The V-I characteristics are shown in Figure 2.29. At 1kPa a normal glow discharge was observed for all DGs with nearly constant V_d (Figure 2.25a). At 50 kPa, (similar to solid anodes at atmospheric pressure) the observed discharge can be broken down into three regimes with increasing I_d: (1) NCG regime (blue shaded region) which transitions to (2) the S-SD regime (red shaded region) followed by (3) the N-SFGD regime (green shaded region). The slope of V_d and I_d (dV_d/dI_d) stays positive for DC NCD regime and starts decreasing as the I_d approaches onset of S-SD regime. Similar to solid anodes listed in Table 2.2 (deposited metal surface anodes) sparks are generated (accompanied by streamers) for DG of 6 mm leading to longer error bars in V_d and I_d (Figure 2.29b). Similar to solid anodes listed in Table 2.2 for DGs of 2 mm and 4 mm streamers were observed, however no current pulses were captured by the current probe. The S-SD regime transitions to a N-SFGD upon further increase in I_d.

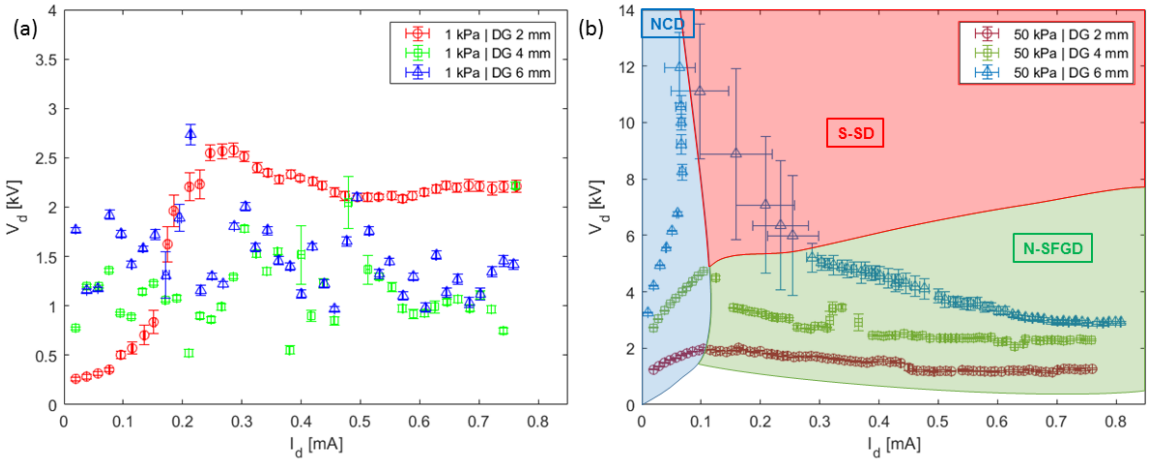

Figure 2.29 V-I characteristics of (a) a normal glow discharge at 1 kPa and (b) NCD regime (blue shaded region), S-SD regime (red shaded region) and N-SFGD regime (green shaded region) at 50 kPa for solid anode Cu1 (Table 2.1).

2.5. Chapter Summary

DC plasma discharges were investigated in a pin-to-plate electrode configuration in air at atmospheric pressure and at sub-atmospheric pressures. A set of solid anode surfaces of different roughness, surfaces of different materials and liquid anodes of different polarity and conductivity were chosen. They were electrical, optically and spacially characterized. The DC plasma discharges on solid anodes were nominally broken down into three regimes with increasing I_d: the NCD regime, the S-SD regime and the N-SFGD regime. S-SD was not observed for solid anodes with smaller surface roughness (< 5 nm) at DGs of 2 mm and 4 mm. NCDs were observed to have a conical diffuse glow closer to anode surface effecting the chemistry and texture of the solid anode. Solid anodes treated under the diffuse glow were characterized using surface roughness measurement, wetting tests, adhesion tests and X-ray photoelectron spectroscopy.

Plasma discharges over polar liquid anodes were also broken down into three regimes with increasing I_d: the NCD regime, a transitional regime and the N-SFGD. Plasma discharges over non-polar liquid only appeared to be in the NCD regime with the absence of diffuse glow. A concave liquid meniscus under the cathode was observed for all liquid electrodes.

A custom plasma chamber was built for sub-atmospheric pressure experiments. DC discharges at 1 kPa were observed to operate in a normal glow discharge regime. DC discharges at 50 kPa were broken down into regimes similar to that of DC discharges at atmospheric pressure for solid anodes.

3. NON-EQUILIBRIUM/NON-THERMAL PULSED CORONA DISCHARGE IN AIR, FLUID VAPORS AND LIQUID PHASES

We discuss the characteristics of nano-to-microsecond pulsed corona discharges in air, fluid vapors and liquid phases in this chapter. We use an external double spark gap circuit to characterize the pulses and report the pulsed discharge characteristics in this section in various fluids.

3.1. Experimental Setup

3.1.1. Double spark gap circuit

An external circuit was used to generate a pulsed plasma discharge in different fluid phases. The pulse generator is a two spark gap circuit mentioned in the literature [10, 28, 76]. The external circuit allowed the variation of the pulsed discharge characteristics (*i.e.*, pulse V_d and duration of pulse)

Figure 3.1 shows the external circuit used to generate the pulsed discharges. A negative polarity DC power source was connected in series with a ballast resistor (50 MΩ) and the DG. A capacitor bank (2 nF) is placed in parallel with the power source and the DG. Voltage and current probes were connected to the pin electrode (cathode) and were used to measure the V_d and I_d. The waveforms from voltage and current probes were captured by an oscilloscope. The external circuit contains two spark gaps, the first spark gap (SG1) breaks down when the electric field is higher than the breakdown electric field for the gas in which it is operating (~31 kV/cm for air for experiments in this thesis). SG1 delivers voltage to the load (plasma discharge) while a second spark gap (SG2) removes

the voltage from the load (extinguishes the discharge). The length of SG1 controls the pulse V_d, while the length of SG2 controls the pulse duration of the discharge. Smaller values of SG2 will extinguish the discharge sooner leading to smaller pulse duration and vice versa. Combination of power source voltage, the value of ballast resistor and the capacitor determines the frequency of the pulse.

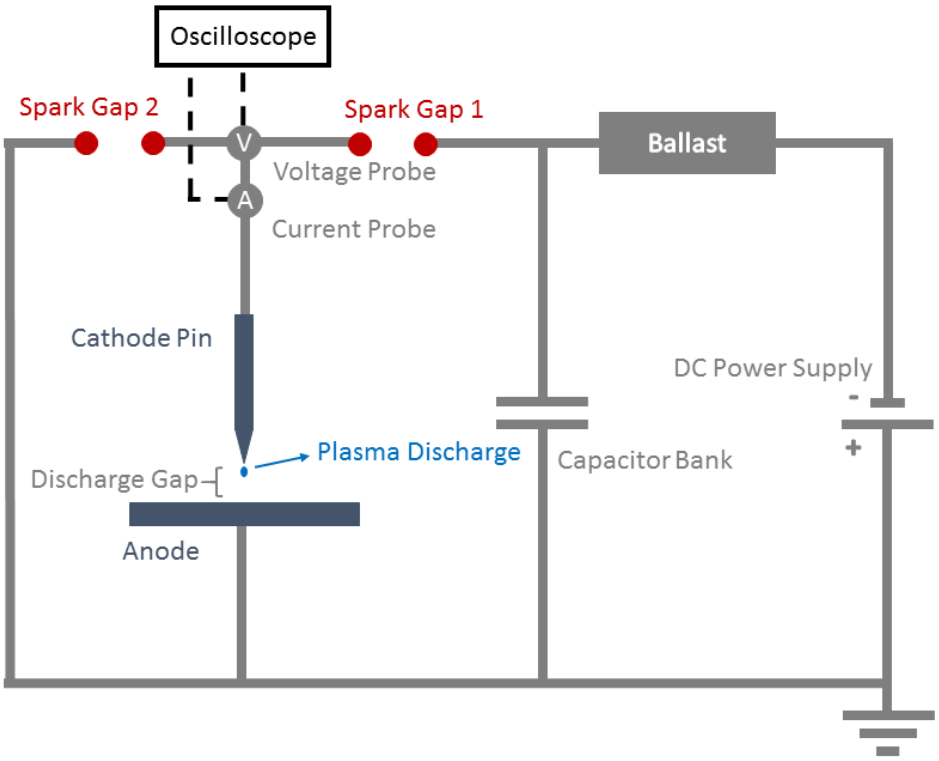

Figure 3.1 Double spark gap circuit used to generate pulsed plasma discharge in fluids. SG1 and SG2 represents the two spark gaps. The thick solid lines represents the connections in the circuit. Dashed lines are the BNC cables connecting the voltage and current probe to the oscilloscope.

A pin to plate electrode configuration is used for the spark gaps. The pins are fabricated from solid copper rods with hemispherical ends ≈ 6 cm diameter and plates are made of copper. The circuit was kept compact to prevent unwanted parasitic capacitance and stray inductance which leads to ringing in the pulse signal, however, some ringing was still observed in the V_d waveform (Figure 3.4). Figure 3.2 shows the experimental setup with the components mentioned above.

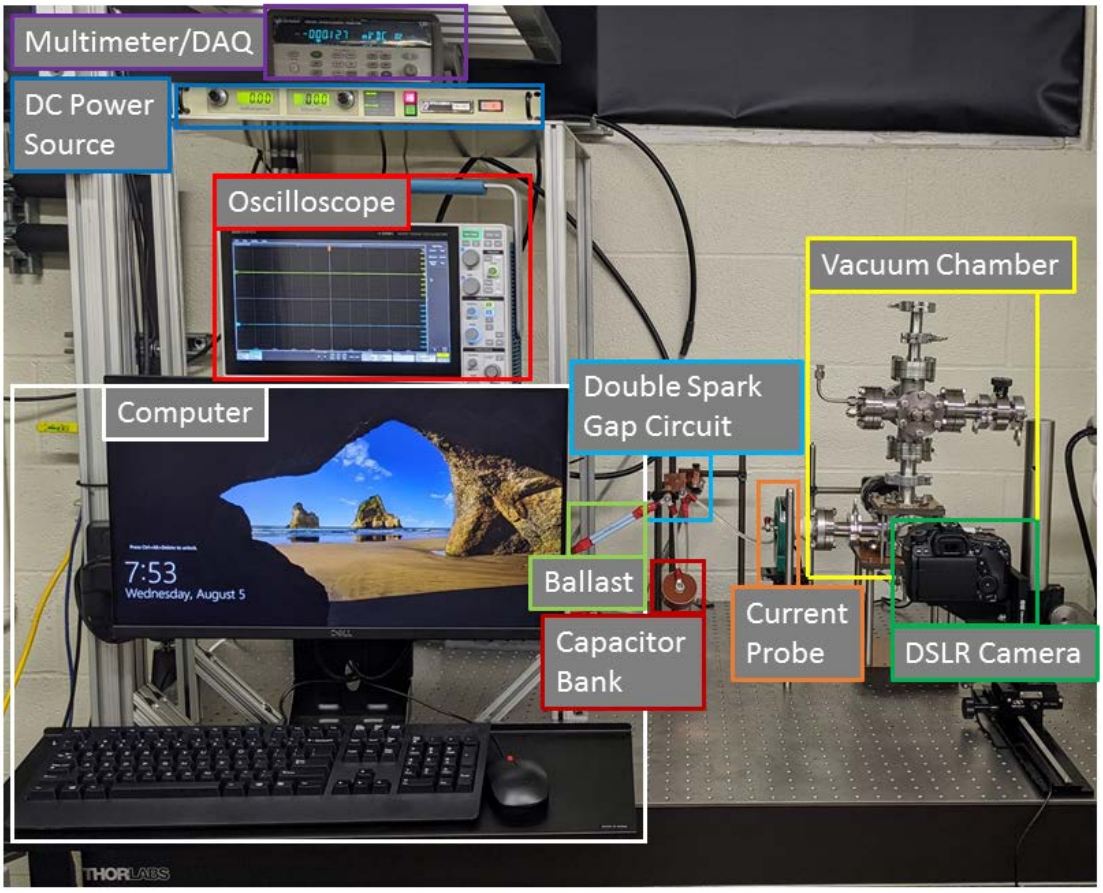

Figure 3.2 Experimental setup with the double spark gap circuit shown in Figure 3.1.

3.2. Pulsed Plasma Discharge at Atmospheric Pressure

The double spark gap circuit (Figure 3.1) is capable of variable pulse duration and V_d. In order to understand the operation of the circuit, it was characterized for a combination of different lengths of the two spark gaps with discharges generated in air, de-ionised water and silicone Oil (viscosity 10cSt) at atmospheric pressure. A wire was inserted into the liquid to ground it (approximate DG ≈ 15 mm). To study the effect of SG1, the length of SG2 was kept constant at 2 mm and length of SG1 was varied from 1 mm to 10 mm. At values of SG1 > SG2 both spark gaps are discharged with pulse durations in nanoseconds and a corona like discharge (homogenous glow) formed at/near the sharp electrode (*i.e*. cathode). This is referred to as the "normal pulsing mode" (Figure 3.3). At values SG1 < SG2 only SG1 discharges resulting in a longer pulse duration, and a brighter and more non-uniform discharge, this is referred to as the "stepped voltage mode".

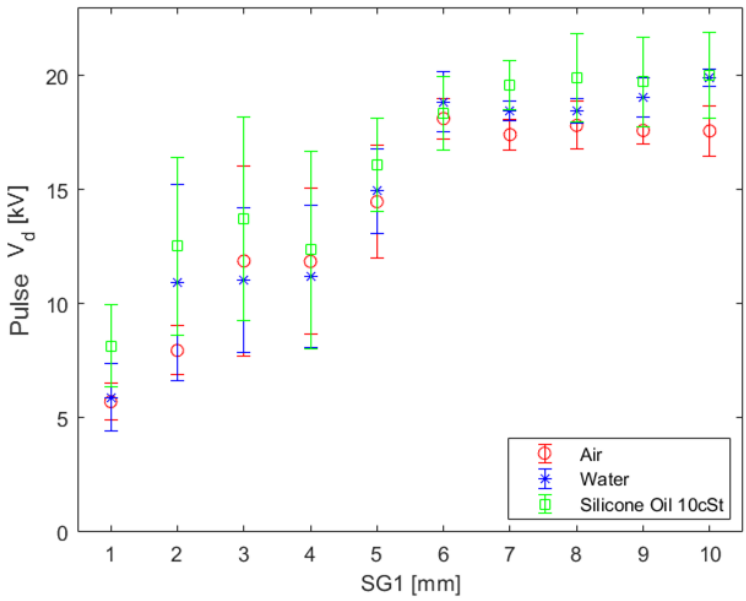

Figure 3.3 Pulse V_d for pulsed discharges in air, water and silicone oil at atmospheric pressure keeping the length of SG2 constant at 2 mm and varying the length of SG1.

The effect of SG2 on the discharge was also characterized by keeping SG1 constant at 6 mm and varying the length of SG2 from 1 mm to 5 mm. Figure 3.4 shows voltage and current waveform for discharges in water. The pulse duration was estimated from the full width half maximum (Figure 3.5). The pulse duration increased from ~12 ns to ~30 ns. This was consistent for all the fluids tested.

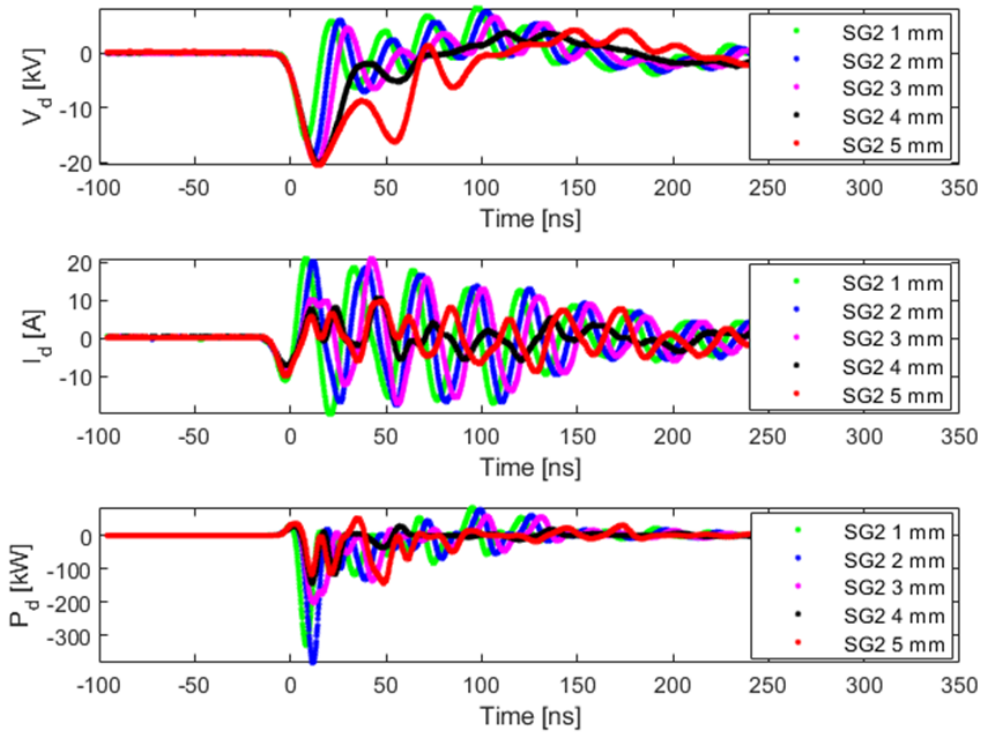

Figure 3.4 Waveforms of V_d, I_d and discharge power ($P_d = V_d \cdot I_d$) obtained for pulsed discharges in water at atmospheric pressure keeping the length of SG1 constant at 6 mm and varying the length of SG2.

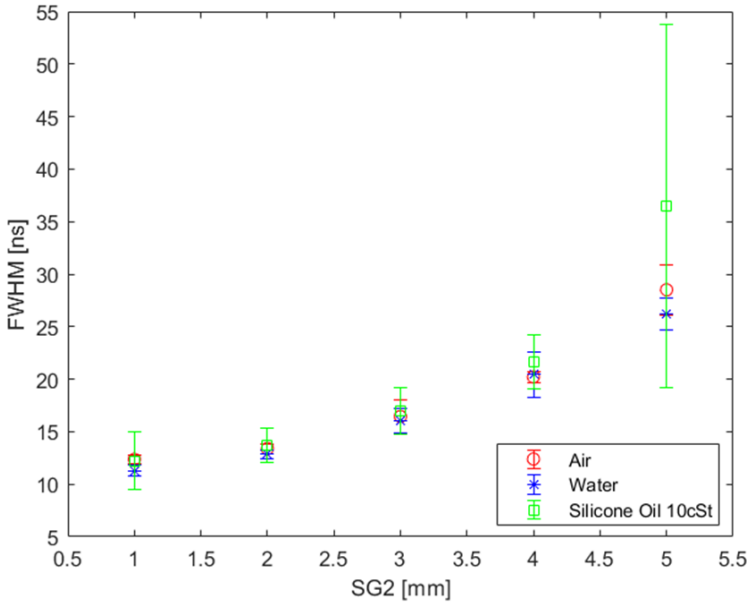

Figure 3.5 Full Width Half maximum (pulse duration) of pulsed discharges in air, water and silicone oil at atmospheric pressure keeping the length of SG1 constant at 6 mm and varying the length of SG2.

The images of discharges obtained by keeping SG1 constant at 6 mm and varying SG2 from 1 mm to 5 mm are presented in Figure 3.6. Though the discharge intensity is low it appears as a bright spot at the tip of the cathode. The images are accumulation of ≈40 discharges.

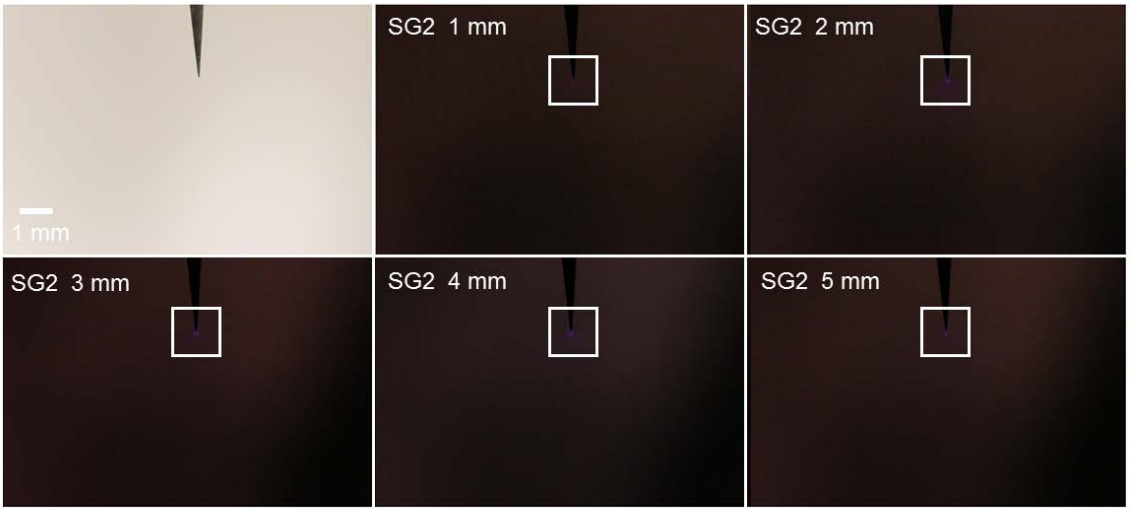

Figure 3.6 Images of pulsed corona discharges (white box) in air at atmospheric pressure keeping the length of SG2 constant at 6 mm and varying the length of SG1 Exposure time of images is 15 s. The negative pin electrode is at the top of the image. Images are accumulation of ≈ 40 pulses.

Figure 3.7 shows the total energy of the pulse for cases where SG1 is kept constant at 6 mm and SG2 is varied from 1 mm to 5 mm. The total energy of the pulse is calculated from the total power of the pulse (instantaneous power for the waveform is shown in Figure 3.4) by integrating the discretized waveform of power in time (Figure 3.4). The pulse energy is in mJ, indicating that non-thermal discharges are generated.

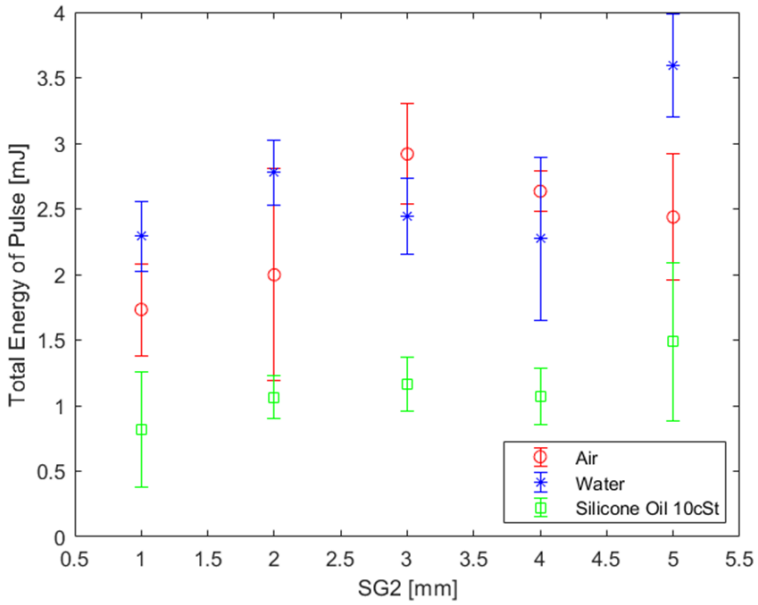

Figure 3.7 Total Energy of pulsed discharges in air, water and silicone oil at atmospheric pressure keeping the length of SG1 constant at 6 mm and varying the length of SG2.

3.3. Pulsed Plasma Discharges in Sub-atmospheric Pressure

Similar to pulsed corona discharges in liquids at atmospheric pressure, the effect of SG2 on the discharges was also characterized for pulsed discharges in air at sub-atmospheric pressure of 2 kPa and 50 kPa and pure water vapor at 2.6 kPa and mixture of water vapor and air at 50 kPa. These experiments were conducted inside the vacuum chamber (Figure 2.2) with cathode and anode connected to the external circuit via the high voltage feedthrough and the ground electrodes. For experiments with water vapor, a vacuum pump was used to create vacuum conditions, and, prior to evacuating the chamber, a droplet of water was placed inside the chamber. The decreasing pressure decreases the boiling point of water. The water droplet starts boiling, leading to decrease in temperature of the droplet and eventually it freezes. After the water droplet freezes and the pressure

reaches below 100 Pa, the vacuum valve was closed and the droplet was passively heated till the temperature inside the chamber reached ambient temperature (22 °C) and a pressure of 2.6 kPa. Since the saturation pressure of water at 22 °C is 2.646 kPa, this procedure ensured that the chamber was filled with pure water vapor. For experiments with a mixture of water vapor and air at a pressure of 50 kPa, after first following the pure water vapor experimental procedure described above, air was inserted into the chamber increasing its pressure to 50 kPa.

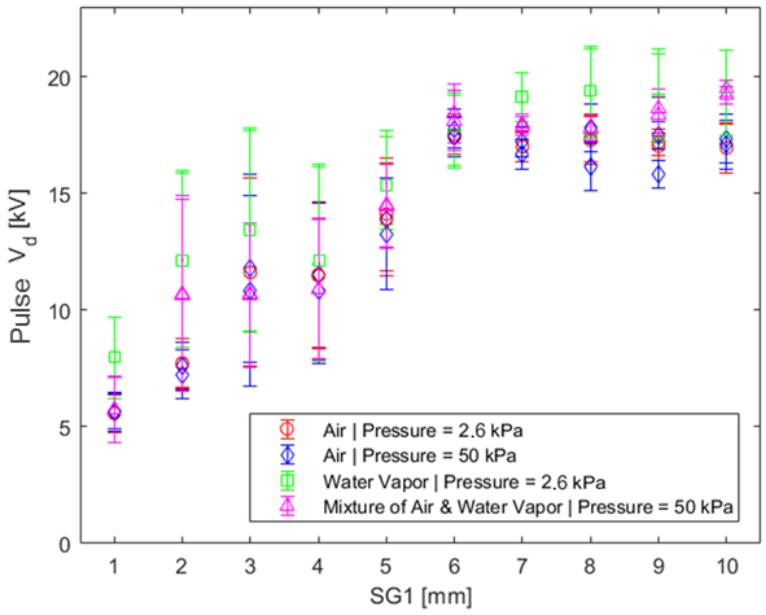

Figure 3.8 Pulse V_d for pulsed discharges in air, water vapor, and, mixture of air and water vapor at sub-atmospheric pressures keeping the length of SG2 constant at 2 mm and varying the length of SG1.

Figure 3.8 and Figure 3.9 shows the pulse V_d and FWHM respectively for air, water vapor, and, mixture of air and water vapor at sub-atmospheric pressures. The spark

gap characteristics are similar to that of liquids at atmospheric pressure (Figure 3.3). For discharges at 50 kPa, a corona spot was visible for both air, and, mixture of water vapor and air (Figure 3.10). At lower pressure of ~2 kPa, glow discharge was observed where the cathode was completely illuminated for both air and pure water vapor.

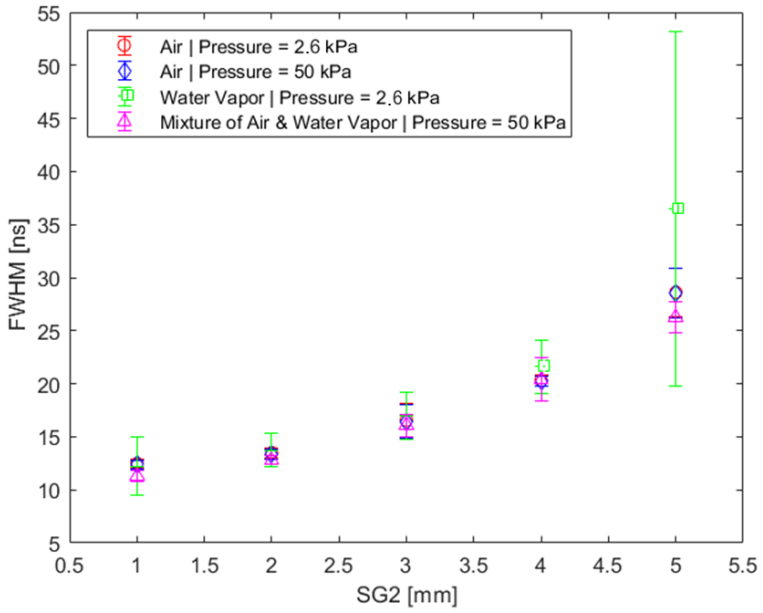

Figure 3.9 Full Width Half maximum (pulse duration) for pulsed discharges in air, water vapor, and, mixture of air and water vapor at sub-atmospheric pressures keeping the length of SG1 constant at 6 mm and varying the length of SG2.

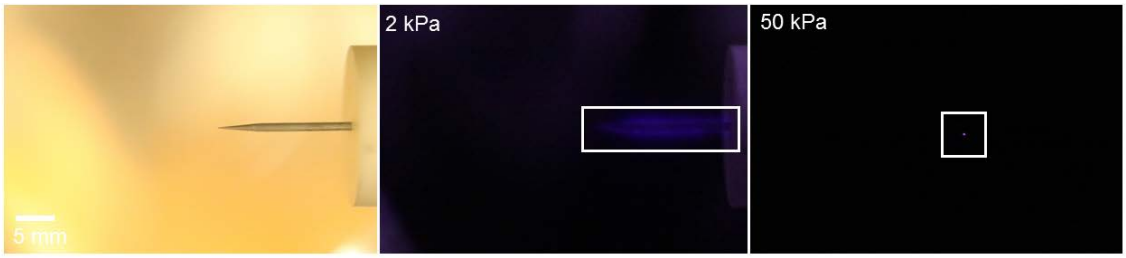

Figure 3.10 Images for pulsed discharges (white box) in air at sub-atmospheric pressure. Here, SG1 = 6 mm and SG2 = 2 mm. Exposure time of image is 1 s. Images are accumulation of ≈3 pulses.

3.4. Chapter Summary

A pulse generator using two spark gaps was used to generate nano-to-micro second pulsed corona discharge in air, fluid vapors and liquid phases. The external circuit facilitated the variation of the pulsed discharge characteristics (*i.e.*, pulse V_d and duration of pulse) for different fluids (with varying polarity and conductivity) at atmospheric pressure. The discharges were characterized at sub atmospheric pressures for air, water vapor and their mixture. The discharges were also characterized optically.

4. CONCLUSIONS AND RECOMMENDATION FOR FUTURE WORK

4.1. Conclusions

DC plasma discharges were operated in air at atmospheric pressure and sub-atmospheric for pin (cathode) – to – plate (anode) electrode configuration. Discharges were operated at I_d upto 0.8 mA. The effect of the interaction of the plasma with solid surfaces anode of different roughness, solid anode surfaces of different materials, and, polarity and conductivity of liquid anodes was studied. DC plasma discharges were electrically, optically and spatially characterized. The presence of diffuse glow in negative corona discharge (NCD) regime only requires a conductive anode, it exists on anodes of different materials and surface roughness. The diffuse glow was observed for both solid (Table 2.1 and Table 2.2), and polar liquid anodes (water and formamide). Formation of sparks (streamer-spark discharge, S-SD) is dependent on the anode surface roughness, discharge gap (DG) and the operating pressure. It is more prominent in rough surfaces with larger discharge gaps and pressure. Contrary to rough anodes, sparks were not observed for ultra smooth anodes for DGs of 2 mm and 4 mm at atmospheric pressure. Sparks were also not observed at DGs of 2 mm and 4 mm at sub-atmospheric pressure of 50 kPa for rougher anode Cu1 (Table 2.1 and Table 2.2).

Anode surfaces were also treated in the NCD operating regime with the diffuse glow. X-ray photoelectron spectroscopy revealed the formation of anode material oxides due to the treatment. Micro/nano structures were also formed on the anode surfaces. Thin metal films of Al, Cu and Ni were damaged at the center of the diffuse glow, resulting in

the adhesive Ti layer or the Si substrate being exposed. This was potentially due to the presence of the moving constriction in that region. The constriction likely oxidized the anode surface, and the resulting metal oxides potentially have poor adhesion to the solid anode. The higher oxidation potential of Al, Cu and Ni is potentially responsible for higher oxidation rates compared to Au and Pt. A combination of adhesion tests (Ar plasma treatment, lint free cloth wiping and ASTM D3359 tape test) revealed poor adhesion of structures formed on the Si substrate, and, on Au and Pt metal films. The roughness of surfaces increased after treatment in the diffuse glow NCD regime. The wettability of anodes with smooth and ultra-smooth surfaces also increased after plasma treatment.

A double spark gap external circuit was built to generate pulsed corona discharges. Electrical characterization of the pulsed discharges indicated that the discharge characteristics were independent of the operational fluid (liquid, vapor or air), but dependent on the operating pressure.

4.2. Recommendation for Future Work

The study of atmospheric DC NCG has demonstrated the possibility of applying corona discharges for materials processing. However, these studies were preliminary and further optimization of the discharge is required to completely understand the breakdown mechanisms and apply plasma discharge to materials processing.

The constriction observed within the diffuse glow in NCD regime can potentially be the result of rapid pulsing. A modified experimental setup equipped with alternative current probe, and a photo multiplier tube (PMT) or intensified charge-coupled device (ICCD) camera may be used to capture this pulsing constriction.

The change in relaxation time of liquid and the voltage drop inside the liquid was also not considered in the voltage-current characteristics, an experimental study could be re-conducted to obtain refined voltage V-I voltage-current characteristics.

The structures formed on plasma treated Si, Au100 and Pt100 could be potentially due to the impurities (oil and water vapor) present in the air. Experiments can be repeated in an environmental chamber in presence of clean artificial air to characterize the effect of impurities or water vapor present in the air on the surface features and/or oxides formed.

The rate of thin film oxidation also needs to be further investigated. The thickness of oxides on anode surfaces is also non-uniform and varies from the center to the edges of the diffuse glow. The fabrication of micro/nano structures for different anode surfaces can also be characterized. A study can be conducted looking into the geometry of the anode to enhance or to make uniform oxide formations.

REFERENCES

1. Fridman, A. and L.A. Kennedy, *Plasma physics and engineering*. 2004, Boca Raton: CRC press.
2. Golovin, I. and B. Kadomtsev, *State and prospects of controlled thermonuclear synthesis.* Atomnaya Ehnergiya, 1996. **81**(5): p. 364-372.
3. Makabe, T. and Z.L. Petrovic, *Plasma electronics: Applications in microelectronic device fabrication*. Vol. 26. 2014, Boca Raton: CRC Press.
4. Waymouth, J.F. and F. Bitter, *Analysis of the plasma of fluorescent lamps.* Journal of Applied Physics, 1956. **27**(2): p. 122-131.
5. Kazemi, M.A., D.S. Nobes and J.A. Elliott, *Effect of the thermocouple on measuring the temperature discontinuity at a liquid–vapor interface.* Langmuir, 2017. **33**(28): p. 7169-7180.
6. Kazemi, M.A., D.S. Nobes and J.A. Elliott, *Investigation of the phenomena occurring near the liquid–vapor interface during evaporation of water at low pressures.* Physical Review Fluids, 2018. **3**(12): p. 124001.
7. Jafari, P., A. Amritkar and H. Ghasemi, *Temperature discontinuity at an evaporating water interface.* The Journal of Physical Chemistry C, 2019. **124**(2): p. 1554-1559.
8. Gatapova, E.Y., I.A. Graur, O.A. Kabov, V.M. Aniskin, M.A. Filipenko, et al., *The temperature jump at water–air interface during evaporation.* International Journal of Heat and Mass Transfer, 2017. **104**: p. 800-812.

9. Fang, G. and C. Ward, *Temperature measured close to the interface of an evaporating liquid.* Physical Review E, 1999. **59**(1): p. 417.

10. Antao, D.S., D.A. Staack, A. Fridman and B. Farouk, *Atmospheric pressure dc corona discharges: Operating regimes and potential applications.* Plasma Sources Science and Technology, 2009. **18**(3): p. 035016.

11. Goossens, O., T. Callebaut, Y. Akishev, A. Napartovich, N. Trushkin, et al., *The dc glow discharge at atmospheric pressure.* IEEE Transactions on Plasma Science, 2002. **30**(1): p. 176-177.

12. Akishev, Y., M. Grushin, I. Kochetov, V. Karal'Nik, A. Napartovich, et al., *Negative corona, glow and spark discharges in ambient air and transitions between them.* Plasma Sources Science and Technology, 2005. **14**(2): p. S18.

13. Xu, L., Z. Fang, P.a. Song and M. Peng, *Effects of corona discharge on the surface structure, morphology and properties of multi-walled carbon nanotubes.* Applied Surface Science, 2010. **256**(21): p. 6447-6453.

14. Bian, X., L. Chen, D. Yu, L. Wang and Z. Guan, *Surface roughness effects on the corona discharge intensity of long-term operating conductors.* Applied Physics Letters, 2012. **101**(17): p. 174103.

15. Bian, X., L. Chen, D. Yu, L. Wang and Z. Guan, *Impact of surface roughness on corona discharge for 30-year operating conductors in 500-kv ac power transmission line.* IEEE Transactions on Power Delivery, 2012. **27**(3): p. 1693-1695.

16. Lee, J.H., H.G. Kim, G.S. Khang, H.B. Lee and M.S. Jhon, *Characterization of wettability gradient surfaces prepared by corona discharge treatment.* Journal of Colloid Interface Science, 1992. **151**(2): p. 563-570.

17. Podgorski, L., B. Chevet, L. Onic and A. Merlin, *Modification of wood wettability by plasma and corona treatments.* International Journal of Adhesion and Adhesives, 2000. **20**(2): p. 103-111.

18. Popelka, A., I. Novák, M.A.S. Al-Maadeed, M. Ouederni and I. Krupa, *Effect of corona treatment on adhesion enhancement of lldpe.* Surface Coatings Technology, 2018. **335**: p. 118-125.

19. Blais, P., D. Carlsson and D. Wiles, *Effects of corona treatment on composite formation. Adhesion between incompatible polymers.* Journal of Applied Polymer Science, 1971. **15**(1): p. 129-143.

20. Owens, D., *Mechanism of corona–induced self-adhesion of polyethylene film.* Journal of Applied Polymer Science, 1975. **19**(1): p. 265-271.

21. Huang, J., J. Zhang and L. Wang, *Review of vapor condensation heat and mass transfer in the presence of non-condensable gas.* Applied Thermal Engineering, 2015. **89**: p. 469-484.

22. Sparrow, E. and S. Lin, *Condensation heat transfer in the presence of a noncondensable gas.* Journal of Heat Transfer, 1964. **86**(3): p. 430-436.

23. Al-Diwany, H. and J. Rose, *Free convection film condensation of steam in the presence of non-condensing gases.* International Journal of Heat and Mass Transfer, 1973. **16**(7): p. 1359-1369.

24. Van Doornmalen, J. and K. Kopinga, *Measuring non-condensable gases in steam.* Review of Scientific Instruments, 2013. **84**(11): p. 115106.

25. Peterson, P. and C. Tien, *Miniature wet-bulb technique for measuring gas concentrations in condensing or evaporating systems.* Experimental Heat Transfer, 1987. **1**(1): p. 1-15.

26. He, J., G. Lin, L. Bai, J. Miao, H. Zhang, et al., *Effect of non-condensable gas on startup of a loop thermosyphon.* International Journal of Thermal Sciences, 2013. **72**: p. 184-194.

27. Wen, R., X. Zhou, B. Peng, Z. Lan, R. Yang, et al., *Falling-droplet-enhanced filmwise condensation in the presence of non-condensable gas.* International Journal of Heat and Mass Transfer, 2019. **140**: p. 173-186.

28. Staack, D., A. Fridman, A. Gutsol, Y. Gogotsi and G.J.A.C. Friedman, *Nanoscale corona discharge in liquids, enabling nanosecond optical emission spectroscopy.* 2008. **120**(42): p. 8140-8144.

29. Townsend, J.S., *Electricity in gases*. 1915, Moscow: Рипол Классик.

30. Fridman, A., A. Chirokov and A. Gutsol, *Non-thermal atmospheric pressure discharges.* Journal of Physics D: Applied Physics, 2005. **38**(2): p. R1.

31. Pai, D.M. and B.E. Springett, *Physics of electrophotography.* Reviews of Modern Physics, 1993. **65**(1): p. 163.

32. Mizuno, A., *Electrostatic precipitation.* IEEE Transactions on Dielectrics Electrical Insulation, 2000. **7**(5): p. 615-624.

33. Vandenbroucke, A.M., R. Morent, N. De Geyter and C. Leys, *Non-thermal plasmas for non-catalytic and catalytic voc abatement.* Journal of Hazardous Materials, 2011. **195**: p. 30-54.

34. Carroll, D., I. Dzidic, R. Stillwell, K. Haegele and E. Horning, *Atmospheric pressure ionization mass spectrometry. Corona discharge ion source for use in a liquid chromatograph-mass spectrometer-computer analytical system.* Analytical Chemistry, 1975. **47**(14): p. 2369-2373.

35. Hadji, K., F. Pontiga, A. Belasri, S. Hadj-Ziane and A. Fernández-Rueda, *Experimental study of ozone generation by negative corona discharge in mixtures of n2 and o2.* Ozone: Science Engineering, 2014. **36**(1): p. 65-72.

36. Pignolet, P., S. Hadj-Ziane, B. Held, R. Peyrous, J. Benas, et al., *Ozone generation by point to plane corona discharge.* Journal of Physics D: Applied Physics, 1990. **23**(8): p. 1069.

37. Pontiga, F., C. Soria, A. Castellanos and J.D. Skalny, *A study of ozone generation by negative corona discharge through different plasma chemistry models.* Ozone: Science Engineering, 2002. **24**(6): p. 447-462.

38. Yamamoto, T., P.A. Lawless and L.E. Sparks, *Triangle-shaped dc corona discharge device for molecular decomposition.* IEEE Transactions on Industry Applications, 1989. **25**(4): p. 743-749.

39. Bussiahn, R., R. Brandenburg, T. Gerling, E. Kindel, H. Lange, et al., *The hairline plasma: An intermittent negative dc-corona discharge at atmospheric pressure for plasma medical applications.* Applied Physics Letters, 2010. **96**(14): p. 143701.

40. Scholtz, V., J. Julák, V. Kríha and J. Mosinger, *Decontamination effects of low-temperature plasma generated by corona discharge. Part i: An overview.* Prague Med Rep, 2007. **108**(2): p. 115-27.

41. Scholtz, V., J. Julák, V. Kríha, J. Mosinger and S. Kopecká, *Decontamination effects of low-temperature plasma generated by corona discharge. Part ii: New insights.* Prague Med Rep, 2007. **108**(2): p. 128-146.

42. Lama, W. and C. Gallo, *Systematic study of the electrical characteristics of the``trichel''current pulses from negative needle-to-plane coronas.* Journal of Applied Physics, 1974. **45**(1): p. 103-113.

43. Trichel, G., *The mechanism of the negative point to plane corona near onset.* Physical Review, 1938. **54**(12): p. 1078.

44. Chang, J.-S., P.A. Lawless and T. Yamamoto, *Corona discharge processes.* IEEE Transactions on Plasma Science, 1991. **19**(6): p. 1152-1166.

45. Giao, T.N. and J. Jordan, *Trichel streamers and their transition into the pulseless glow discharge.* Journal of Applied Physics, 1970. **41**(10): p. 3991-3999.

46. He, Q., Z. Zhu and S. Hu, *Flowing and nonflowing liquid electrode discharge microplasma for metal ion detection by optical emission spectrometry.* Applied Spectroscopy Reviews, 2014. **49**(3): p. 249-269.

47. Magureanu, M., N.B. Mandache and V.I. Parvulescu, *Degradation of pharmaceutical compounds in water by non-thermal plasma treatment.* Water Research, 2015. **81**: p. 124-136.

48. Chen, Q., J. Li, Y. Li, S. Yang and X. Zhang, *Plasma-liquid interaction: A new way to synthesize nanomaterials*. 2014.

49. Horikoshi, S. and N. Serpone, *In-liquid plasma: A novel tool in the fabrication of nanomaterials and in the treatment of wastewaters.* RSC Advances, 2017. **7**(75): p. 47196-47218.

50. Boussetta, N. and E. Vorobiev, *Extraction of valuable biocompounds assisted by high voltage electrical discharges: A review*. Comptes Rendus Chimie, 2014. **17**(3): p. 197-203.

51. Kumar, S., R. Singh, T. Singh and B. Sethi, *Surface modification by electrical discharge machining: A review.* Journal of Materials Processing Technology, 2009. **209**(8): p. 3675-3687.

52. Hijosa-Valsero, M., R. Molina, A. Montràs, M. Müller and J.M. Bayona, *Decontamination of waterborne chemical pollutants by using atmospheric pressure nonthermal plasma: A review*. Environmental Technology Reviews, 2014. **3**(1): p. 71-91.

53. Kim, J.-H., M.-A. Lee, G.-J. Han and B.-H. Cho, *Plasma in dentistry: A review of basic concepts and applications in dentistry.* Acta Odontologica Scandinavica, 2014. **72**(1): p. 1-12.

54. Tanaka, H., K. Ishikawa, M. Mizuno, S. Toyokuni, H. Kajiyama, et al., *State of the art in medical applications using non-thermal atmospheric pressure plasma.* Reviews of Modern Plasma Physics, 2017. **1**(1): p. 3.

55. Aller, L.H.J.a., *Astrophysics. The atmospheres of the sun and stars.* 1963.

56. Duguet, T., V. Fournée, J. Dubois and T. Belmonte, *Study by optical emission spectroscopy of a physical vapour deposition process for the synthesis of complex alcufe (b) coatings.* Surface Coatings Technology, 2010. **205**(1): p. 9-14.

57. De Jong, M. and N. Rowlands, *Proton beam diagnostics using optical spectroscopy.* Nuclear Instruments Methods in Physics Research Section B: Beam Interactions with Materials Atoms, 1985. **10**: p. 822-824.

58. Curtis, B. and H. Brunner, *End point determination of aluminum ccl4 plasma etching by optical emission spectroscopy.* Journal of Electrochemical Society, 1978. **829**.

59. Pongrác, B., M. Šimek, M. Člupek, V. Babický and P. Lukeš, *Spectroscopic characteristics of h α/oi atomic lines generated by nanosecond pulsed corona-like discharge in deionized water.* Journal of Physics D: Applied Physics, 2018. **51**(12): p. 124001.

60. Staack, D., A. Fridman, A. Gutsol, Y. Gogotsi and G. Friedman, *Nanoscale corona discharge in liquids, enabling nanosecond optical emission spectroscopy.* Angewandte Chemie International Edition, 2008. **47**(42): p. 8020-8024.

61. Bruggeman, P. and C. Leys, *Non-thermal plasmas in and in contact with liquids.* Journal of Physics D: Applied Physics, 2009. **42**(5): p. 053001.

62. Bruggeman, P.J., M.J. Kushner, B.R. Locke, J.G. Gardeniers, W. Graham, et al., *Plasma–liquid interactions: A review and roadmap.* Plasma Sources Science and Technology, 2016. **25**(5): p. 053002.

63. Vanraes, P. and A. Bogaerts, *Plasma physics of liquids—a focused review*. Applied Physics Reviews, 2018. **5**(3): p. 031103.

64. Griem, H.R., A.C. Kolb and K. Shen, *Stark broadening of hydrogen lines in a plasma*. Physical Review, 1959. **116**(1): p. 4.

65. Lisitsa, V.S., *Stark broadening of hydrogen lines in plasmas.* Soviet Physics Uspekhi, 1977. **20**(7): p. 603.

66. Dobrynin, D., Y. Seepersad, M. Pekker, M. Shneider, G. Friedman, et al., *Non-equilibrium nanosecond-pulsed plasma generation in the liquid phase (water, pdms) without bubbles: Fast imaging, spectroscopy and leader-type model.* Journal of Physics D: Applied Physics, 2013. **46**(10): p. 105201.

67. *Labview*. 2020, National Instruments.

68. Jameel, R., Y. Wu, Y. Wu and K. Pratt, *Primary standards and standard reference materials for electrolytic conductivity*. NIST Special Publication, 2000. **1**: p. 142-260.

69. University, T.A.M. *Material characterization facility*. 2020 [cited 2020 8/29/20]; Available from: https://mcf.tamu.edu/.

70. University, T.A.M. *Aggiefab nanofabrication facility*. 2020 [cited 2020 8/20/2020]; Available from: https://aggiefab.tamu.edu/.

71. Wilson, A., D. Staack, T. Farouk, A. Gutsol, A. Fridman, et al., *Self-rotating dc atmospheric-pressure discharge over a water-surface electrode: Regimes of operation.* Plasma Sources Science and Technology, 2008. **17**(4): p. 045001.

72. Bruggeman, P., J. Liu, J. Degroote, M.G. Kong, J. Vierendeels, et al., *Dc excited glow discharges in atmospheric pressure air in pin-to-water electrode systems.* Journal of Physics D: Applied Physics, 2008. **41**(21): p. 215201.

73. Yabe, A., Y. Mori and K. Hijikata, *Ehd study of the corona wind between wire and plate electrodes.* AIAA journal, 1978. **16**(4): p. 340-345.

74. Davis, J.A., R.O. James and J.O. Leckie, *Surface ionization and complexation at the oxide/water interface: I. Computation of electrical double layer properties in simple electrolytes.* Journal of Colloid Interface Science, 1978. **63**(3): p. 480-499.

75. Haynes, W.M., *Handbook of chemistry and physics*. 2014, Boca Raton: CRC press.

76. Mankowski, J. and M. Kristiansen, *A review of short pulse generator technology.* IEEE Transactions on Plasma Science, 2000. **28**(1): p. 102-108.